S. D'amico, J.-S. Ardaens, G. Gaias, H. Benninghoff, B. Schlepp, J.L. Jorgensen
Noncooperative Rendezvous Using Angles-Only Optical Navigation: System Design and Flight Results
Journal of Guidance Control and Dynamics, Vol. 36, N. 6, 2013, p. 1576-1595
doi:10.2514/1.59236

Non-Cooperative Rendezvous using Angles-only Optical Navigation: System Design and Flight Results

S. D'Amico[1], J.-S. Ardaens[2], G. Gaias[3], H. Benninghoff[4], B. Schlepp[5]
German Aerospace Center (DLR), Münchner Str. 20, 82234 Wessling, Germany

J.L. Jørgensen[6]
DTU Space, Elektrovej, Building 327, DK-2800 Lyngby, Denmark

This paper presents system design and on-orbit results from the Advanced Rendezvous Demonstration using GPS and Optical Navigation (ARGON) which has been conducted during the extended phase of the PRISMA mission in April 2012. The ARGON experiment has been motivated by the new generation of on-orbit-servicing and debris-removal missions which are discussed at national and international level. Its primary goal was to demonstrate the capability of an active servicer spacecraft to safely approach and rendezvous a non-cooperative passive client using angles-only optical navigation in a ground-in-the-loop fashion. To this end, a dedicated flight dynamics system has been developed for routine processing of the camera images collected on-board, for estimation of the relative orbit of the servicer with respect to the client vehicle, for maneuver planning and commanding. Despite the inherent difficulty to estimate the actual range to target through angles-only measurements and the constraints affecting the communication between ground-station and servicer, ARGON demonstrated an efficient and safe rendezvous from 30 km to the final hold point at 3 km mean separation selected before experiment start. This was possible due to the achieved relative navigation accuracy in combination with a guidance strategy based on the relative eccentricity/inclination vector separation method. As shown in the paper, the availability of independent and precise navigation information from carrier-phase differential GPS gave the possibility to properly evaluate the achieved performance and cross-compare different relative navigation sensors after the conclusion of the technology demonstration.

Nomenclature

Abs	=	Absolute value
ARGON	=	Advanced Rendezvous demonstration using GPS and Optical Navigation
CCD	=	Charge-Coupled Device
CHU	=	Camera Head Unit
CNES	=	French National Space Center
DARPA	=	U.S.'s Defense Advanced Research Projects Agency
DEOS	=	DEutsche Orbitale Servicing mission
DLR	=	German Aerospace Center
DTU	=	Danish Technical University
ECC	=	Experiment Control Center
ESRANGE	=	Esrange Space Center
GHOST	=	GPS High precision Orbit determination Software Tools

[1] Lead Research Engineer, GSOC/Space Flight Technology, Münchner Str. 20, 82234 Wessling, Germany.
[2] Research Engineer, GSOC/Space Flight Technology, Münchner Str. 20, 82234 Wessling, Germany.
[3] Research Engineer, GSOC/Space Flight Technology, Münchner Str. 20, 82234 Wessling, Germany.
[4] Research Engineer, GSOC/Space Flight Technology, Münchner Str. 20, 82234 Wessling, Germany.
[5] Research Engineer, GSOC/Space Flight Technology, Münchner Str. 20, 82234 Wessling, Germany.
[6] Professor, DTU Space, Elektrovej, Building 327, DK-2800 Lyngby, Denmark.

GNC	=	Guidance, Navigation, and Control
GPS	=	Global Positioning System
GRAPHIC	=	GRoup And PHase Ionospheric Correction
GSOC	=	German Space Operations Center
IMP	=	Image Processing
JPEG	=	Joint Photographic Experts Group
MAP	=	MAneuver Planning
MCC	=	Mission Control Center
N	=	Cross-track
NORAD	=	North American Aerospace Defense Command
PLUTO	=	Procedure Language for Users in Test and Operations
POD	=	Precise Orbit Determination
PRISMA	=	Prototype Research Instruments and Space Mission technology Advancement
R	=	Radial
RMS	=	Root-Mean-Square
ROD	=	Relative Orbit Determination
ROI	=	Region of Interest
RTN	=	Radial/Along-track/Cross-track orbital frame
SNSB	=	Swedish National Space Board
Std	=	Stdandard deviation
s/c	=	Spacecraft
T	=	Along-track
TanDEM-X	=	TerraSAR-X-Add-on for Digital Elevation Measurements
TC	=	Telecommand
TLE	=	Two Line Elements
TM	=	Telemetry
UTC	=	Universal Time Coordinated
VBS	=	Vision-Based Sensor
2D	=	Two-Dimensional
3D	=	Three-Dimensional

I. Introduction

This work is mainly motivated by the new generation of on-orbit-servicing and debris-removal missions which are under consideration by several national and international space agencies. Key examples are Orbital Express [1], commissioned by the U.S.'s Defense Advanced Research Projects Agency (DARPA) and successfully launched in March 2007, or the DEutsche Orbitale Servicing Mission (DEOS) of the German Aerospace Center (DLR) [2], which is in the preliminary design phase. These projects and others are driving the demand to efficiently approach, rendezvous, inspect, and dock non-cooperative on-orbit objects. Strategic applications of this technology are in the frame of space situational awareness (e.g., debris detection, inspection and removal), orbital lifetime prolongation/extension (e.g., refueling, repair, take over of attitude and orbit control functionalities), and science (e.g., Mars and Titan sample return missions) among others.

Common to these missions is the necessity to approach a non-cooperative passive target from large distances (e.g., > 30 km) in a fuel efficient, safe, and accurate manner. This poses new challenges as compared to the most recent on-orbit demonstrations given by TanDEM-X [3] and PRISMA [4]. In these missions, the usage of relative GPS techniques is necessary to estimate and autonomously control the relative motion between the co-orbiting spacecraft. As a consequence, the adoption of an inter-satellite link for communication and a high degree of collaboration between the chaser (or servicer) and target (or client) vehicles is usually required to accomplish the objectives.

Measurement techniques alternative to GPS have been used in the past for rendezvous navigation. Relevant examples are the radar systems used for the Gemini, Apollo, Shuttle programs and Soyuz-Type spacecraft, or lidar instruments as embarked on the XSS-11 flight demonstration by the U.S. Air Force Research Laboratory [5]. Although these sensors can provide relative range and angle measurements to the target, they place significant power and weight requirements on the servicer spacecraft design. Furthermore these sensor systems are active and

can not be adopted for stealthy operations. On the contrary, many simple passive low cost sensors can provide line-of-sight direction, such as optical or infrared cameras. In fact, many spacecraft are now equipped with star trackers which, if properly oriented, can be used to track a space object within its field of view. Indeed this type of sensor is considered as a very attractive solution to perform relative navigation tasks based on angles-only measurements [6].

The potential of angles-only navigation for orbital rendezvous has been recognized by various authors in the past [7—12]. Raja Chari [7] analyzed the performance of angles-only navigation during close proximity operations through Kalman filtering and linear covariance. More realistic scenarios have been studied by Dave Woffinden [8] through six-degrees of freedom simulations. However, range estimates were derived from apparent diameter measurements to the target object. Jason Schmidt [9] expanded the concept through high-fidelity simulations for analysis without availability of any range information. Hemanshu Patel [10] exploited the concept of partial observability, and showed how characteristics of the relative motion such as shape and orientation can be determined from angles-only measurements even if the full relative state is unobservable. Finally, to the authors knowledge, the only published on-orbit demonstrations of angles-only navigation for autonomous rendezvous have been conducted in the frame of the Swedish PRISMA mission [11, 12].

This work expands on the previous literature and demonstrates ground-based, far-range rendezvous to a non-cooperative and unknown client using angles-only navigation in the frame of a flight experiment conducted in April 23-27, 2012 during PRISMA [13]. In contrast to previous flight demonstrations, here an attempt has been made to generalize the rendezvous strategy and improve the portability and applicability of the developed techniques to other missions. The primary instrument used for angles-only navigation is the Vision-Based Sensor (VBS) of the Danish Technical University (DTU) embarked on the active Mango spacecraft [7]. This is used for vision-based navigation of Mango with respect to the passive Tango, which act respectively as servicer and client vehicles during the experiment. Despite the availability of advanced features for autonomous relative navigation offered by the VBS system (e.g., automatic identification and tracking of non-stellar objects), here the camera head for far-range navigation (i.e., a common star tracker) is used only to collect images. These are stored on-board, later down-linked during ground-contacts, and finally processed on-ground to extract line-of-sight information for relative navigation. During the experiment, the servicer spacecraft body axes are aligned with the local orbital frame in such a way that the VBS camera is always oriented in (anti-)flight direction. On the other hand, the client spacecraft rotates with an angular velocity of ca. 0.12 deg/s (i.e., two revolutions per orbit), in order to emulate a slowly tumbling passive object. Furthermore, in order to mimic a representative scenario, no a-priori knowledge of the target vehicle is used during the experiment apart from Two-Line-Elements (TLEs) delivered by the North American Aerospace Defense Command (NORAD) [14]. As shown in the paper, the precise relative orbit determination products based on carrier-phase differential GPS [15] are only used post-facto after the experiment conclusion to assess the accuracy of the navigation and control tasks. All these features are unique to the on-orbit demonstration described in this paper.

In order to fulfill the experiment objectives, a flight dynamics system has been specifically developed which is characterized by numerous innovations as compared to the existent literature. The parameterization of the relative motion is based on the relative eccentricity and inclination vectors [16], which are used for the first time to enhance angles-only navigation and exploit the system properties of partial observability. In contrast to earlier approaches, the estimated relative state includes relative orbital elements instead of the usual relative position and velocity components. This approach decouples the state components to a large extent and allows a straightforward separation of observable and unobservable parameters. Since the non-observability of the system is mainly condensed in the relative mean argument of latitude, the shape of the relative motion can be determined from the early phases of the approach based on the observable relative orbital elements [17]. This early knowledge of the geometry enables safe approaches simply by setting a proper relative eccentricity and inclination vector separation [18]. At the same time, the estimation error of the relative mean argument of latitude can be decreased through the execution of a dedicated maneuver profile as described in the paper.

In addition to the deeper geometrical insight, the usage of relative orbital elements offers several advantages in the design and implementation of a non-cooperative far-range rendezvous. First of all, Earth oblateness effects due to J_2 can be easily included in the dynamics of relative motion. This simplifies the implementation of a navigation filter and its eventual integration into an on-board computer with limited computational capacity. Second, the estimated relative orbital elements can be used right away and consistently for deterministic maneuver planning, based on the Gauss' variational equations [19]. Third the usage and interpretation of the relative orbit determination and maneuver planning software are largely simplified for operators because they deal with slowly varying features

of the relative motion such as shape and orientation rather than the constantly varying Hill's position and velocity coordinates [20]. It is noted that short-range and docking scenarios (<100 m separation) are not addressed in this paper. In these cases, especially during forced motion control activities, the advantages of a parameterization in terms of the relative orbital elements may partially vanish. Still contingency situations involving collision avoidance or escape maneuvers can profit from the relative eccentricity/inclination vector separation concept [16,18].

An iterative batch least squares filtering scheme has been adopted in this paper for relative orbit determination. This is the most suitable strategy in the context of a ground-based operational scenario. The processing of the complete history of data by means of multiple iterations enables a more powerful data editing than achievable through sequential techniques. In addition the errors in dynamics modeling are not absorbed by the process noise, which allows deeper insight into the systematic errors [21]. A fundamental challenge faced by angles-only navigation is the inherent difficulty to accurately determine the range to target. In rigorous terms, the navigation problem becomes observable only in the presence of orbit control maneuvers which change the relative orbit geometry of the formation [22]. At large separations, the instantaneous change of the relative motion induced by a maneuver can not be detected by a star tracker. Thus the overall system observability has to be assessed considering the average change of the formation geometry over longer time spans, typically multiples of the orbital revolution. Throughout the experiment, orbit control maneuvers are planned on-ground and executed regularly by the servicer to track a pre-defined guidance profile. The guidance profile is specifically designed to realize the desired rendezvous while ensuring system observability, safety, fuel efficiency, and the presence of the client in the field of view (i.e., visibility).

This introduction is followed by an overview of the PRISMA mission, spacecraft and the Advanced Rendezvous demonstration using GPS and Optical Navigation (ARGON). The third section is focused on a description of the developed flight dynamics system and its key algorithms. The experiment plan and its operational concept are given in the fourth section. The fifth section presents the flight results obtained during ARGON, including image processing, and performance assessment of the relative navigation and control tasks. The sixth and final section is dedicated to the lessons learned, way forward, and the potential applications of this novel technology to current and future strategically relevant missions.

II. On-Orbit Testbed

The ARGON experiment has been conceived, designed, and executed by the German Space Operations Center (GSOC) of DLR during the extended phase of the Swedish PRISMA mission. The related spacecraft operations have been conducted in the time frame April 23-27, 2012 by two teams of engineers, respectively from DLR/GSOC and from OHB-Sweden (OHB-SE), which were collocated at the PRISMA mission control center in Stockholm/Solna, Sweden. A detailed description of PRISMA and its goals can be found in [23, 24]. After briefly recalling the mission and spacecraft, this chapter provides a description of the VBS system and the primary goals of ARGON.

A. PRISMA

The Prototype Research Instruments and Space Mission technology Advancement (PRISMA) consists of two spacecraft, namely Mango and Tango (see Fig. 1). In the following, the spacecraft are often referred to as servicer and client due the respective roles played during the ARGON experiment. The Mango spacecraft is 3-axis stabilized via star trackers and reaction wheels and is equipped with a propulsion system providing full 3D orbit control capability independent from the attitude. Tango is also 3-axis stabilized through a solar-magnetic attitude control system, but does not have any orbit control capability. On June 15, 2010, the two spacecraft were launched clamped together into a 720/780 km altitude dawn-dusk sun-synchronous orbit. After an initial period of commissioning, Tango was separated and successfully acquired on August 11, 2010. The mission includes the flight qualification of several sensor and actuator systems as well as the in-flight execution of a range of guidance, navigation, and control (GNC) experiments using this equipment [13]. OHB-SE is the prime contractor for the project which is funded by the Swedish National Space Board (SNSB). The German Aerospace Center (DLR), the French National Space Center (CNES) and the Technical University of Denmark (DTU) provide additional support in terms of on-board software and hardware contributions. Among the numerous GNC experiments conducted by the participating organizations, this paper addresses the ARGON on-orbit demonstration of DLR/GSOC.

The PRISMA satellites are operated from the OHB-SE premises in Stockholm/Solna, Sweden using a ground antenna of the Esrange Space Center (ESRANGE) in Kiruna, Sweden. In combination with the spacecraft orbit, this results in late afternoon and nighttime passages with up to 10 passages per day. The Mission Control Center (MCC) is based on the in-house developed RAMSES ground control system [25]. For approximately five months, between March and August 2011, the mission was operated by DLR/GSOC in order to prolong its operational lifetime. A cloned MCC was set up at DLR/GSOC and personnel were trained at OHB-SE. In addition to the Kiruna antenna, DLR/GSOC also made use of ground stations in Weilheim, Germany and Inuvik, Canada. This allowed for an increased amount of passages and day-time operations [26].

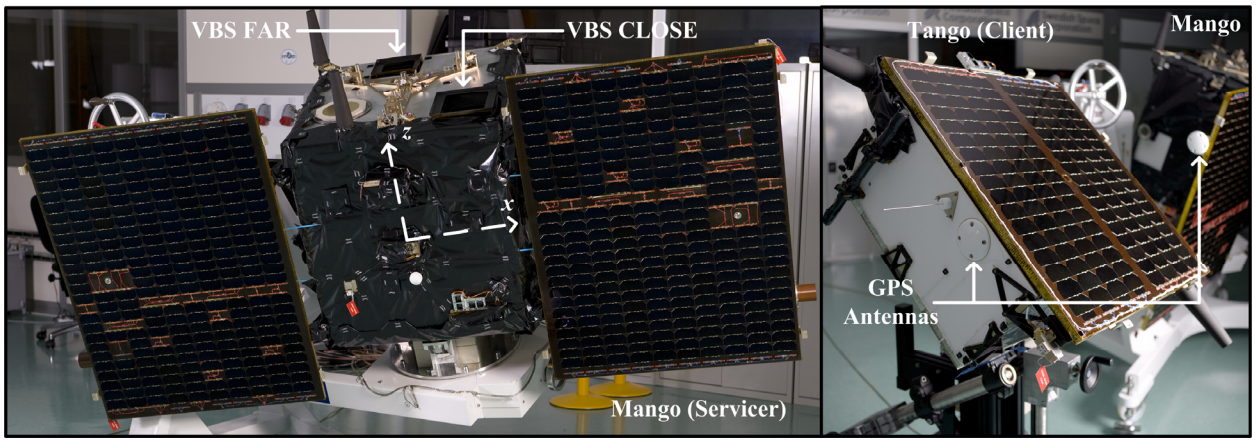

Figure 1. PRISMA Mango (left) and Tango (right) spacecraft flight models before launch. The VBS far-/close-range cameras and the GPS antennas are indicated in white. The Mango body axes are represented by dashed arrows. Courtesy of OHB-SE.

B. Vision-Based Sensor (VBS)

The optical navigation system embarked on the PRISMA mission and used for this research is based on the microASC platform, a fully autonomous miniature star sensor (see Fig. 2) [27]. In its general configuration, the microASC is designed for high flexibility and can host from one to four Camera Head Units (CHU). These can be located at suitable places and directions on a spacecraft, such that a fully redundant blinding free attitude sensor configuration can be achieved.

On-board the Mango servicer vehicle, two CHUs are used as standard attitude sensors. Their pointing directions are selected such that simultaneous blinding by Sun and Earth is avoided during the complex fly-around maneuvers. The third port on the microASC is also equipped with a standard CHU. This can be pointed in the forward or backward directions (c.f., z-axis in Fig. 1), such that the client Tango can be seen in the field of view for most of the mission phases. The fourth port is equipped with a CHU characterized by a modified focal length and iris, to enable operations at close range with strong light conditions. These latter CHUs feature an electronic shutter control for improved dynamic range and are used for vision-based navigation of Mango with respect to Tango during PRISMA experiment operations. Fig. 1 depicts the two CHUs, which are named VBS FAR and VBS CLOSE.

During ARGON, VBS FAR has been used exclusively for angles-only navigation, and only for imaging purposes. Although the camera works as a normal star tracker and processes the obtained images to deliver a star-based attitude, this functionality has not been used in this work. In addition, the camera features a process which automatically extracts so-called regions of interest (ROIs) defined around the most luminous objects (typically 2-20 ROIs per image). The ROIs are stored in the mass memory of the servicer on-board computer for later download during ground-contacts. Only occasionally, instead of the ROIs, full images from VBS FAR in Joint Photographic Experts Group (JPEG) compressed format have been collected during ARGON. Examples of such images are provided in Fig. 2 (right) as obtained close to the experiment start and end times respectively on April 23 and 27, 2012. These specific images show two representative scenarios which had to be considered during ARGON. First, at a distance of more than 30 km, Tango is seen as a faint dot in the starry sky. Some stars may be detected with an apparent luminosity which is higher than the one reflected by the client spacecraft. This is the case for the first image collected during ARGON (c.f., Fig. 2 – top/right), where the star Vega is clearly the brightest visible object. Second, as the servicer approaches and the range is reduced (<10 km), the client luminosity increases and forces the

activation of the camera shutter to avoid bloomed images. Due to the automatic tuning of the exposure time, the stars are no longer detectable. This occurs in the second image shown in Fig. 2 – bottom/right. Obviously, the different possible behaviors of the star tracker need to be properly handled by a relative navigation task, either implemented on-board or on-ground such as during ARGON. On one hand, the availability of an inertial camera orientation based on the stars from the same image removes biases deriving from uncertainties in the camera parameters and alignment. On the other hand, when stars are underexposed, the relative navigation task has to be able to process line-of-sight information measured directly on the Charge-coupled Device (CCD) plane, i.e. relative to the local camera system, rather than the inertial reference frame. In this case the inertial attitude of the spacecraft has to be retrieved from the standard on-board star trackers and combined with the a-priori knowledge of the VBS FAR camera orientation in body frame.

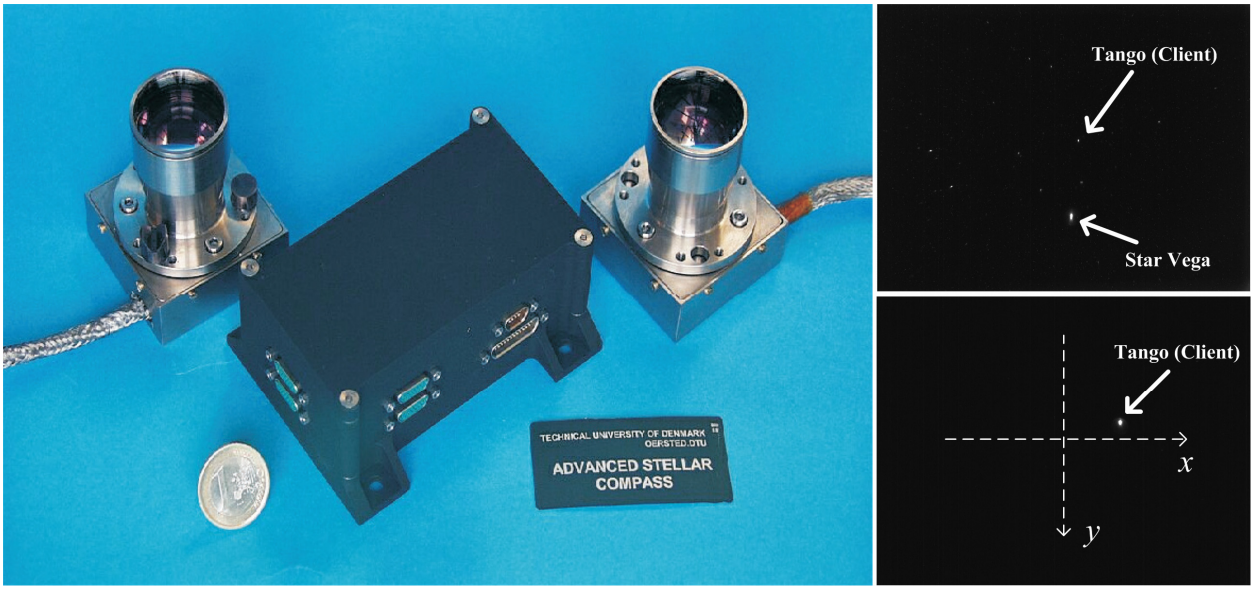

Figure 2. MicroASC digital processing unit pictured with two camera heads (left) [27]. Example compressed images taken by the Mango far-range camera (VBS FAR, c.f. Fig. 1) during ARGON close to the start (April 23, 2012 – top/right) and end (April 27, 2012 – bottom/right) of the experiment. The camera axes are represented by dashed arrows with origin on the CCD geometric center.

A list of key parameters of the VBS FAR camera is provided in Table 1. The position of the CCD geometric center is expressed in the body axes defined in Fig. 1. The camera axes are nearly aligned with the spacecraft body axes, and their relative orientation is parameterized through a quaternion according to the Wertz convention [28]. The applied camera model compensates for the radial distortion introduced by lens effects and is described in [29]. In particular, it takes into account the displacement between the CCD geometric center and the optical axis, the non-quadratism effects, and the lens distortion through a correction which is a function of the radial distance in the CCD plane. The field of view, resolution, pixel size, and optical center are provided by Table 1 in camera axes (see Fig. 2).

Table 1. Main parameters of far-range optical camera (VBS FAR) used during ARGON.

Item	Unit/Type	Value
Position in body frame	m	(-0.090 0.247 0.594)
Orientation in body frame	quaternion	(0.00519 -0.00182 0.00084 0.99998)
Half field of view	deg	(9.15 6.85)
Camera resolution	pixel	(752 580)
Sun exclusion angle	deg	50
Moon exclusion angle	deg	10
Pixel size	m	$(8.6\ \ 8.3)\cdot10^{-6}$
Optical axis in CCD plane	pixel	(20 -1)
Lens distortion coefficient	ad	$2.6\cdot10^{-8}$
Effective focal length	m	$20187\cdot10^{-6}$

C. Advanced Rendezvous using GPS and Optical Navigation (ARGON)

ARGON has been conceived primarily to demonstrate man-in-the-loop, far-range rendezvous to a non-cooperative, passive, and unknown client using vision-based navigation. The key capabilities which had to be demonstrated by ARGON are listed in the following:

- Handover of servicer operations from NORAD TLEs to angles-only navigation at large separations.
- Planning and execution of safe unambiguous guidance strategies for far-range rendezvous.
- Collection, analysis, and processing of far-range camera images during rendezvous.
- Routine orbit determination and maneuver calibration of servicer s/c based on GPS measurements.
- Routine relative orbit determination (client vs. servicer) based on angles-only measurements.
- Ground-based maneuver planning and execution to track the desired guidance profile.
- Acquisition of hold no-drift point at a prescribed mean along-track separation from the client.

It is noted that all tasks described above had to rely only on data of the servicer spacecraft available after downlink ground-contacts. Apart from coarse a-priori information available from the NORAD TLE catalogue, the client vehicle is assumed to be unknown and non-cooperative. Furthermore, the specific autonomous navigation functionalities of the VBS system are ignored to extend the generality and portability of ARGON to a servicer spacecraft equipped with standard star trackers only. The safety and visibility constraints which had to be taken into account in the design of the rendezvous guidance are depicted in Fig. 3.

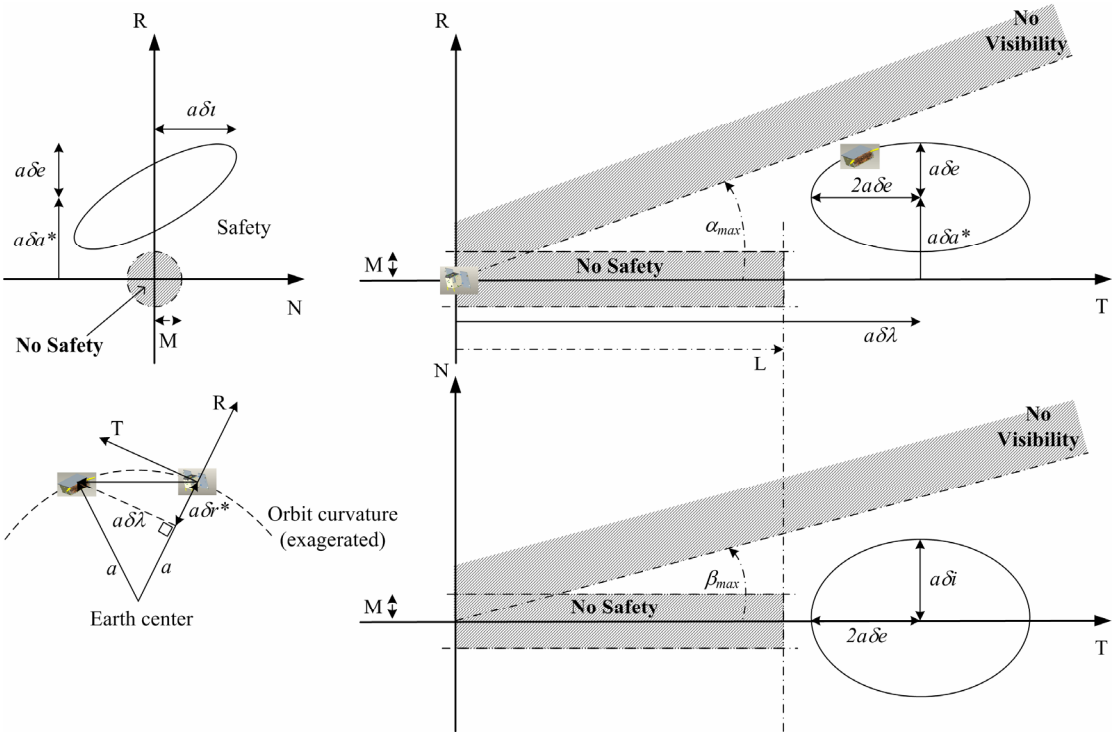

Figure 3. Snapshot of safety and visibility constraints in the orbital frame centered on Mango. An arbitrary relative motion of the client w.r.t. the servicer is projected into the along-track/radial (top/right), along-track/cross-track (bottom/right), and cross-track/radial (top/left) directions. The corresponding relative orbital elements are also indicated. Here, the along-track drift due to the different orbit energies is neglected for visualization purposes. The effect of the orbit curvature is also depicted (bottom/left).

The relative motion of the client vehicle is mapped in the orbital frame centered on the servicer and aligned with the radial (R, positive in Zenith direction), along-track (T, positive in flight direction), and cross-track (N, normal to the orbital plane) directions. The servicer spacecraft body axes can be aligned with the orbital frame in such a way that the VBS FAR camera is always oriented in flight (z = T) or anti-flight (z = -T) direction. The nominal attitude can be selected on-ground depending on the expected location of the client ahead or behind the servicer respectively. The following set of relative orbital elements [16,18]

$$\boldsymbol{x} = \begin{pmatrix} \delta a \\ \delta e_x \\ \delta e_y \\ \delta i_x \\ \delta i_y \\ \delta u \end{pmatrix} = \begin{pmatrix} \delta a \\ \delta e \cos\varphi \\ \delta e \sin\varphi \\ \delta i \cos\vartheta \\ \delta i \sin\vartheta \\ \delta u \end{pmatrix} = \begin{pmatrix} (a - a^{\mathrm{o}})/a^{\mathrm{o}} \\ e\cos(\omega) - e^{\mathrm{o}}\cos(\omega^{\mathrm{o}}) \\ e\sin(\omega) - e^{\mathrm{o}}\sin(\omega^{\mathrm{o}}) \\ i - i^{\mathrm{o}} \\ (\Omega - \Omega^{\mathrm{o}})\sin(i^{\mathrm{o}}) \\ (u - u^{\mathrm{o}}) \end{pmatrix}, \tag{1}$$

is adopted to parameterize the relative motion and to express the aforementioned constraints in a convenient way. Here a, e, i, ω, Ω, and M denote the classical Keplerian elements, whereas $\boldsymbol{e} = (e\cos\omega\ e\sin\omega)^{\mathrm{T}}$, and $u = M + \omega$ represent the eccentricity vector and the mean argument of latitude. The superscript "o" denotes quantities referring to the reference spacecraft which defines the origin of the orbital frame (here the servicer). Under the assumptions of the Hill-Clohessy-Wilshire equations [30], the magnitude of the relative eccentricity and inclination vectors, δe and δi, provide the amplitudes of the in-plane and out-of-plane relative motion oscillations, whereas relative semi-major axis, δa, and relative mean longitude, $\delta\lambda = \delta u + \delta i_y \cot(i^0)$, provide mean offsets in radial and along-track directions respectively [16, 18]. The orientation of the shape of the relative motion is driven by the phase angles φ and θ, which identify the mean argument of latitude of the perigee and ascending node of the relative orbit. For large separations, the relative semi-major axis can be corrected to first order as follows

$$\delta a^* = \delta a + \delta r^* = \delta a + \left(1 - \sqrt{1 - \delta\lambda^2}\right) \approx \delta a - \delta\lambda^2 / 2\,, \tag{2}$$

to take into account the curvature of the orbit when modeling the radial separation. Eq. (2) is derived from simple geometrical considerations applied to Fig. 3 (bottom/left), where δr^* represents the radial correction due to the orbit curvature.

In order to keep visibility, the client spacecraft has to be within the field of view of the VBS FAR camera. According to Fig. 3, this constraint is translated by the following expressions in terms of relative orbital elements

$$\begin{cases} \left|\delta e + \delta a^*\right| / \left|\delta\lambda\right| < \tan(\alpha_{\max}) \\ \delta i / \left|\delta\lambda\right| < \tan(\beta_{\max}) \end{cases}, \tag{3}$$

where $\alpha_{\max}$ and $\beta_{\max}$ represent half fields of view of the camera (see Table 1) in x- and y-axes or equivalently in the directions parallel and perpendicular to the orbit plane under nominal servicer attitude (see Fig. 3). The safety concept is based on the well known relative eccentricity and inclination vector separation method [16, 18]. In the presence of large uncertainties in the along-track separation, such as with angles-only navigation, the collision risk is measured as a function of the radial and cross-track separations. These can be minimized through a formation configuration with (anti-)parallel $\delta\boldsymbol{e}$ and $\delta\boldsymbol{i}$. In this case, the minimum separation perpendicular to the flight direction is given by the vector magnitudes as [16, 18]

$$\delta r_{\mathrm{RN\,min}} = a^0 \min\left(\delta i, \left|\delta e - \left|\delta a^*\right|\right|\right), \tag{4}$$

and the relative motion is considered safe if one of the following conditions is valid

$$\begin{cases} \delta r_{\mathrm{RN\,min}} > \mathrm{M} & \text{for} \quad a^0\delta\lambda < \mathrm{L} \\ \delta r_{\mathrm{RN\,min}} \geq 0 & \text{for} \quad a^0\delta\lambda \geq \mathrm{L} \end{cases}. \tag{5}$$

Here, M represents a safety threshold for the minimum separation perpendicular to the flight direction, whereas L is an along-track separation which shall be selected large enough to provide inherent safety independently from the formation shape, orientation, and the relative navigation errors. The regions of non-visibility and non-safety defined by Eqs. (3, 4) are depicted in Fig. 3 through dashed areas. It is noted that the non-safety region is only violated if the

minimum between the radial and cross-track separations lies within the indicated area. The provided constraints will be used in the next sections to derive a nominal guidance profile and motivate the choice of the desired hold-point aimed by ARGON. This will be possible through the introduction of uncertainties in the relative orbital elements caused by the navigation and control errors expected before experiment start.

III. FLIGHT DYNAMICS SYSTEM

In order to fulfill the objectives and constraints introduced in the previous section a tailored flight dynamics system has been developed for ARGON. This section presents a top level architectural and functional description of the system, including the key concepts and algorithms implemented in the software modules.

A. System Architecture

A simplified architecture layout of the flight dynamics system is illustrated in Fig. 4. The fundamental modules are represented by rectangles with input and output data. The data flows in clockwise direction throughout the closed-loop GNC system. Telemetry data (TM) from the servicer is down-linked during ground-contacts (over ESRANGE), and later processed by the ground-based software. This is used for angles-only relative navigation and subsequent maneuver planning. The resulting Telecommands (TC) are sent back to the servicer spacecraft during up-link contacts for the execution of orbit control maneuvers.

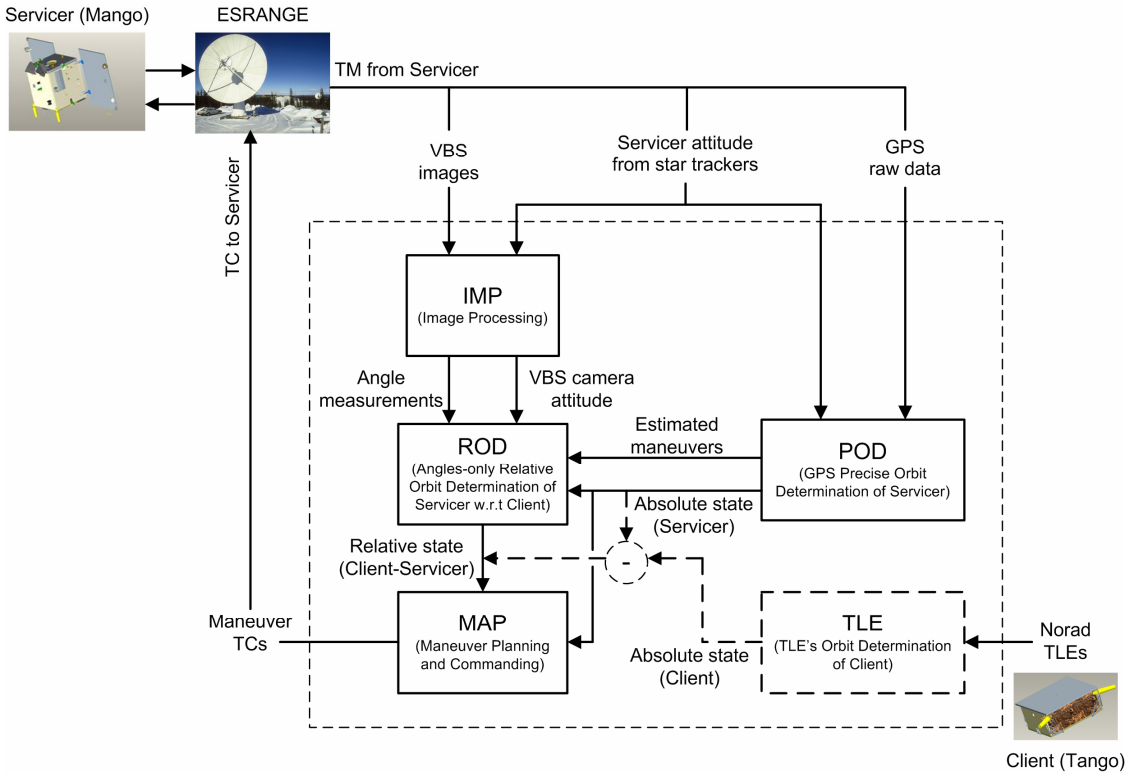

Figure 4. Top-level simplified architecture of flight dynamics system for ARGON.

The Image Processing (IMP) is fed with image and attitude data from the servicer spacecraft. The images are processed to identify the client spacecraft in the field of view and measure its position in the CCD coordinates. Upon detection of a sufficient number of stars in the image, IMP is also able to estimate the inertial orientation of the camera in order to compute the line-of-sight direction vector of the client in the J2000 frame. The resulting angle measurements are filtered by the Relative Orbit Determination (ROD) software in a batch least squares approach. In order to estimate the relative orbit of the servicer w.r.t. the client (i.e., a relative state with six elements), ROD needs the orbit control maneuvers (i.e., size and time) executed by the servicer satellite and its absolute orbit. This information is produced by a Precise Orbit Determination (POD) process based on single-frequency GPS raw data of the servicer. In the case of a failure of the POD, or as a backup, coarse orbit information (i.e., GPS receiver

navigation solutions) and a-priori delta-v maneuver information of the servicer can also be directly retrieved from the TM and used by ROD.

The goal of the Maneuver Planning and Commanding (MAP) is to compute orbit control maneuvers of the servicer to track a pre-defined guidance profile. In order to improve the system observability, in-plane and out-of-plane maneuvers are regularly planned upon availability of the ROD output and executed at various locations along the orbit. MAP computes the desired orbit corrections as a function of the difference between the desired (guidance) and estimated (from ROD) relative orbit. The output of MAP consists of time-tagged maneuver commands which can be directly sent to the servicer spacecraft during up-link contacts.

Prior to the activation of the VBS system, or in general in the absence of VBS camera measurements, the coarse relative orbit can be estimated making use of NORAD TLEs for the client and GPS measurements of the servicer. Due to the poor accuracy of the NORAD TLEs, a dedicated software module (TLE) is used to further filter the TLEs available from consecutive days prior to the experiment start. It is noted that the initial conditions of the ARGON experiment were acquired by OHB-SE introducing the typical control errors induced by TLE-only navigation. In an attempt to mimic a representative on-orbit-servicing scenario, the actual initial relative position and velocity of Mango w.r.t. Tango (derived from GPS data) was not known by DLR/GSOC during the experiment.

B. Image Processing (IMP)

During each ground-contact, a sequence of ROIs is downloaded from the servicer spacecraft which covers a time frame of approximately one orbital revolution (~100 min.). The available ROIs are assembled in equivalent images which can be processed by IMP at once as a batch. The fundamental task of IMP is to detect a target non-stellar object (here the client Tango satellite) for each given image and convert its measured position into a line-of-sight vector in the camera frame. Upon availability of a sufficient number of stars in the field of view, the output line-of-sight vector is accompanied by an estimate of the camera inertial attitude which can be used to map it into the J2000 coordinate system. In its core, IMP consists of five key steps which are explained in the following: 1) detection and linking of clusters in the sequence, 2) detection of stars, 3) detection of client, 4) computation of line-of-sight vector, 5) attitude determination.

A cluster is a set of pixels which is considered as an object of interest. The object might be a star, the client, or some other non-stellar object. The cluster detection algorithm scans each image of the sequence and defines a cluster around a point where the brightness of the corresponding pixel exceeds a user-defined threshold. A recursive scheme is then applied which starts at the detected point and marks all pixels in a neighborhood to belong to the cluster as long as their brightness value is greater than a certain cluster growth threshold. Once a set of pixels, S, belongs to the cluster, its center, $\boldsymbol{c}$, is computed as the weighted sum

$$\boldsymbol{c} = \sum_{\boldsymbol{p}\in S} I(\boldsymbol{p})\boldsymbol{p} \Big/ \sum_{\boldsymbol{p}\in S} I(\boldsymbol{p}) = \sum_{\boldsymbol{p}\in S} I(\boldsymbol{p})\boldsymbol{p} \Big/ s \,, \tag{6}$$

where I is the image intensity (or brightness) evaluated at the pixel $\boldsymbol{p}$, and the cluster size is defined as s. This process is called centroiding and is repeated for each image and for each detected cluster.

The detected clusters need to be linked along the complete image sequence. In particular, for each cluster of the current image, a cluster of the previous image is searched which can be linked to it. To this end, two key parameters are monitored, namely the cluster's center position, $\boldsymbol{c}$, and size, s. For two clusters to be linked, both the difference in center position and size have to be smaller than pre-defined thresholds. Note that for far objects, such as stars, the center positions can be evaluated at the same time through a propagation of the cluster of the previous image to the current image time. This is done through the usage of the available attitude information of the servicer vehicle. On the contrary, for near objects such as the client, the movement in the image domain can not be propagated using the servicer attitude. Thus the comparison of the cluster positions across two subsequent images is done against a different threshold. Occasionally more than one cluster of the previous image seems to be an appropriate candidate for linking according to the aforementioned conditions. Therefore a score is used which is indirectly proportional to the above mentioned differences in $\boldsymbol{c}$ and s. Finally the cluster with the highest score among all clusters of the previous image is linked to the cluster of the current image.

At this stage the star detection is performed employing the Hipparcos star catalogue which contains the location of more than 100,000 stars given in right ascension, α, and declination, δ, w.r.t. J2000 [31]. The direction vector (unit vector) which points from the origin of the J2000 coordinate system to the star is given by

$$\boldsymbol{u}_{\mathrm{J2000}} = \begin{pmatrix} \cos\delta\cos\alpha \\ \cos\delta\sin\alpha \\ \sin\delta \end{pmatrix}, \tag{7}$$

and its transformation to the camera frame results from

$$\boldsymbol{u}_{\mathrm{Cam}} = \boldsymbol{R}^{\mathrm{Cam}}_{\mathrm{Body}}\boldsymbol{R}^{\mathrm{Body}}_{\mathrm{J2000}}\boldsymbol{u}_{\mathrm{J2000}} = \boldsymbol{R}\boldsymbol{u}_{\mathrm{J2000}}\,. \tag{8}$$

Here, the rotation from J2000 to the body frame is given by the servicer attitude quaternion (available from the standard star tracker), whereas the rotation from the body axes to the camera coordinate system is provided in Table 1. The resulting rotation matrix from J2000 to the camera frame is denoted by $\boldsymbol{R}$. The direction vector $\boldsymbol{u}_{\mathrm{Cam}}$ is converted to pixel coordinates, $\boldsymbol{c}^*$, using the DTU camera model which takes into account lens distortion effects (see Table 1) [29]. Only stars within the camera field of view are retained in the calculations, thus a check is done to verify that the pixel lies within the image domain. A cluster in the image can be assigned to a star if the difference between the center of the cluster $\boldsymbol{c}$ and the theoretical pixel position $\boldsymbol{c}^*$ is smaller than a predefined tolerance value. The clusters detected as stars are used for two purposes. First, a cluster assigned to a star cannot be the client. Secondly, the stars associated to each image are stored for later attitude determination.

For each pair of linked clusters, ${}_i\boldsymbol{c}_j$ and ${}_{i-1}\boldsymbol{c}_k$, the motion vector is defined as the difference vector $\Delta_i\boldsymbol{c}_j = {}_i\boldsymbol{c}_j - {}_{i-1}\boldsymbol{c}_k$, where i denotes the image index under consideration, $j \in (0,\ldots,j^{\max})$ is the cluster index of the image i, and $k = k(j)$ is the cluster index of the previous image, i-1, which is linked to cluster j. Since we expect the client to have a different apparent motion vector as compared to the stars, the target is detected by maximizing the following quantity for a given image i

$$\max_j \left[\left\| {}_i\Delta\boldsymbol{c}_j \right\| - \frac{1}{j^{\max}} \sum_{j=1}^{j^{\max}} \left\| {}_i\Delta\boldsymbol{c}_j \right\| \right], \tag{9}$$

under the constraint that the cluster j is not a star. The detection of the client is completed by a motion consistency check. In particular, in order to be considered continuous and valid, the change in position and velocity between two successive images shall not exceed predefined thresholds. Furthermore the client position is linearly interpolated from the available measurements for images where the detection failed. At this stage the position of the client in 2D pixel coordinates is converted to the following 3D direction vector in the camera coordinate system, $\boldsymbol{u}^{\mathrm{c}}$, using again the DTU camera model

$$\boldsymbol{u}^{\mathrm{c}} = \begin{pmatrix} u^{\mathrm{c}}_{\mathrm{x}} \\ u^{\mathrm{c}}_{\mathrm{y}} \\ u^{\mathrm{c}}_{\mathrm{z}} \end{pmatrix} = \begin{pmatrix} \cos(\psi)\sin(\eta) \\ \sin(\psi) \\ \cos(\psi)\cos(\eta) \end{pmatrix}, \tag{10}$$

where η and ψ represents the azimuth and elevation of the client as seen from the VBS FAR camera. With respect to the camera axes, a positive azimuth angle gives a shift in positive x coordinates, whereas a positive elevation gives a shift in positive y coordinates. Zero azimuth and elevation angles correspond to the optical center of the image (c.f., Fig. 2). Here, x and y axes identify the CCD plane, whereas z is along the boresight direction.

In addition, the far-range image processing software includes an attitude determination functionality. As done for the client position, the DTU camera model is adopted to transform the pixel coordinates of the detected stars, $\boldsymbol{c}$, to 3D direction vectors in the camera coordinate system, $\boldsymbol{u}_{\mathrm{Cam}}$. Given a number of stars $j^* > 1$, an optimal inertial attitude rotation matrix, $\boldsymbol{R}$, is searched which minimizes the loss function

$$J(\boldsymbol{R}) = \sum_{j=1}^{j^*} \omega_j \left\| \left(\boldsymbol{u}_{\mathrm{Cam}\,j} - \boldsymbol{R}\boldsymbol{u}_{\mathrm{J2000}\,j} \right) \right\|^2 , \tag{11}$$

where ω_j is the weight of the jth star vector measurement. Minimizing J can be rewritten in an eigenvector problem for the corresponding quaternion and leads to the so-called $\boldsymbol{q}$-method which is well described in [28]. For each image, the inertial attitude determination is performed if at least four stars are detected (i.e., $j^* > 3$).

C. Relative Orbit Determination (ROD)

The task of ROD is the estimation of the relative orbital elements, $\boldsymbol{x}$, defined by Eq. (1) based on the line-of-sight vectors, $\boldsymbol{u}^{\mathrm{c}}$, defined by Eq. (10) and provided by the image processing module. This is done through an iterative dynamics batch least-squares estimator with a-priori information [21, 32]. The actual measurements processed by ROD are the azimuth, η, and elevation, ψ, angles which subtend $\boldsymbol{u}^{\mathrm{c}}$, and can be computed from Eq. (10) as follows

$$\boldsymbol{z} = \begin{pmatrix} \eta \\ \psi \end{pmatrix} = \begin{pmatrix} \mathrm{atan2}(u_{\mathrm{x}}^{\mathrm{c}}, u_{\mathrm{z}}^{\mathrm{c}}) \\ \mathrm{asin}(u_{\mathrm{y}}^{\mathrm{c}}) \end{pmatrix}. \tag{12}$$

In order to implement the least-squares filter, the nonlinear differential equations governing the relative motion are first linearized about a nominal reference state. The linearization procedure leads to the following system of equations in the presence of control inputs and measurements uncertainties

$$\begin{aligned} \boldsymbol{x}(t) &= \boldsymbol{\Phi}(t,t_0)\boldsymbol{x}(t_0) + \boldsymbol{B}(t,t_0)\Delta\boldsymbol{v}(t_0) \\ \boldsymbol{y}(t) &= \boldsymbol{c}(\boldsymbol{x}(t)) + \boldsymbol{\varepsilon}(t) \end{aligned} , \tag{13}$$

where the 6x6 state transition matrix $\boldsymbol{\Phi}$ relates the 6-dimensional state vector $\boldsymbol{x}(t_0)$ at time t_0 to the state $\boldsymbol{x}(t)$ at time t. The 6x3 control input matrix $\boldsymbol{B}$ expresses the variation of the relative orbital elements at time t caused by an impulsive maneuver $\Delta\boldsymbol{v} = (\Delta v_{\mathrm{R}}\ \Delta v_{\mathrm{T}}\ \Delta v_{\mathrm{N}})^{\mathrm{T}}$ at time t_0 with components in the radial, along-track, and cross-track directions. The modeled angle measurements, $\boldsymbol{y}$, are a non-linear function, $\boldsymbol{c}$, of the state, whose partial derivatives are given by the 2x6 measurement sensitivity matrix $\boldsymbol{C}$. $\boldsymbol{\varepsilon}$ is the two-dimensional vector of uncorrelated measurement errors characterized by a normal distribution with zero mean and covariance $\mathrm{Cov}(\boldsymbol{\varepsilon}) = \boldsymbol{W} = \mathrm{diag}(\sigma^2_{\eta}\ \sigma^2_{\psi})$. The system of equations defined by Eq. (13) is discussed in the following.

Instead of a rigorous numerical integration of the equations of motion, here a simple relative dynamics model has been adopted which captures the most relevant perturbations in low Earth orbit [16, 18]. Under the assumptions of Kepler orbits of equal energy (i.e., $\delta a = 0$), the relative orbital elements are constants of motion (i.e., $\boldsymbol{\Phi} = \mathrm{diag}(1,\ldots 1,)$). When the servicer and client have unequal semi-major axis (e.g., $\delta a > 0$), a change of the relative mean argument of latitude in the time frame $\Delta t = t - t_0$ has to be accounted for. If δa and δu are small quantities (i.e., δa and $\delta u << 1$), this drift can be expressed to first order as $-1.5 n^{\mathrm{o}} \Delta t$, where n^{o} is the mean motion of the servicer. Earth oblateness effects due to J_2 can be easily introduced in the relative dynamics model under the additional assumptions of small magnitudes of the relative eccentricity/inclination vectors (i.e., δe and $\delta i << 1$) and small eccentricity (i.e., $e^{\mathrm{o}} << 1$). The resulting secular variations of the relative orbital elements can be derived from the theory of Brower [33]. In particular, the Earth equatorial bulge causes a rotation of the relative eccentricity vector, $\delta\boldsymbol{e}$, a vertical linear drift of the relative inclination vector, $\delta\boldsymbol{i}$, and a linear drift of δu. These effects are proportional to the elapsed time Δt and J_2 and are expressed through to the following parameters

$$\begin{aligned} \dot{\varphi} &= 1.5\gamma^{\mathrm{o}} n^{\mathrm{o}} \left(5\cos^2 i^{\mathrm{o}} - 1 \right) \\ \gamma^{o} &= 0.5 J_2 \left(\mathrm{R_E} / a^{\mathrm{o}} \right)^2 \end{aligned} , \tag{14}$$

where "o" denotes quantities related to the servicer as usual, and $\mathrm{R_E}$ is the Earth equatorial radius. The superposition of the aforementioned effects provides the state transition matrix as

$$\boldsymbol{\Phi}(t,t_0)=\begin{pmatrix} 1 & 0 & 0 & 0 & 0 & 0 \\ 0 & 1 & -\dot{\varphi}\,\Delta t & 0 & 0 & 0 \\ 0 & \dot{\varphi}\,\Delta t & 1 & 0 & 0 & 0 \\ 0 & 0 & 0 & 1 & 0 & 0 \\ 0 & 0 & 0 & 3\gamma^{o}\sin^{2}(i^{\mathrm{o}})n^{\mathrm{o}}\Delta t & 1 & 0 \\ -1.5n^{\mathrm{o}}\Delta t & 0 & 0 & -12\gamma^{o}\sin(2i^{\mathrm{o}})n^{\mathrm{o}}\Delta t & 0 & 1 \end{pmatrix}. \tag{15}$$

The variation of the relative orbital elements caused by an impulsive maneuver (or an instantaneous velocity change) at time t_0 can be modeled under the same assumptions of our linear relative dynamics. In particular the inversion of the solution of the Hill-Clohessy-Wiltshire equations expressed in terms of relative orbital elements provides the following relationship [16, 18]

$$\boldsymbol{B}(t,t_0)=-\frac{\mathrm{sign}(\Delta t)}{n^{\mathrm{o}}}\begin{pmatrix} 0 & 2 & 0 \\ \sin u_0^{\mathrm{o}} & 2\cos u_0^{\mathrm{o}} & 0 \\ -\cos u_0^{\mathrm{o}} & 2\sin u_0^{\mathrm{o}} & 0 \\ 0 & 0 & \cos u_0^{\mathrm{o}} \\ 0 & 0 & \sin u_0^{\mathrm{o}} \\ -2 & -3n^{\mathrm{o}}|\Delta t| & -\sin u_0^{\mathrm{o}}\cot i^{\mathrm{o}} \end{pmatrix}, \tag{16}$$

where $u_0(t_0)$ identifies the mean argument of latitude of the servicer at the delta-v time. Eq. (16) shows how along-track maneuvers cause instantaneous variations of δa and $\delta \boldsymbol{e}$, radial maneuvers cause instantaneous variations of δu and $\delta \boldsymbol{e}$, whereas cross-track maneuvers affect δu and $\delta \boldsymbol{i}$. It is noted that cross-track maneuvers do not change the mean along-track separation, $\delta\lambda = \delta u + \delta i_y \cot i^0$, because the effects on δu and δi_y cancel out, thus the in-plane and out-of-plane relative motion remain fully decoupled in this formulation.

The partial derivatives of the angle measurements w.r.t. relative orbital elements about the reference state are computed through the application of the following chain rule

$$\boldsymbol{C}(t)=\left.\frac{\partial \boldsymbol{y}}{\partial \boldsymbol{x}}\right|_{\bar{\boldsymbol{x}}}=\left.\frac{\partial \boldsymbol{y}}{\partial \delta \boldsymbol{r}_{J2000}}\right|_{\bar{\boldsymbol{x}}}\cdot\begin{pmatrix}\boldsymbol{R}_{\mathrm{RTN}}^{\mathrm{J2000}} \\ \boldsymbol{R}_{\mathrm{RTN}}^{\mathrm{J2000}}\end{pmatrix}\cdot\left.\frac{\partial \delta \boldsymbol{r}_{\mathrm{RTN}}}{\partial \boldsymbol{x}}\right|_{\bar{\boldsymbol{x}}}=\begin{pmatrix}\left.\frac{\partial \eta}{\partial \delta \boldsymbol{p}_{J2000}}\right|_{\bar{\boldsymbol{x}}}\boldsymbol{R}_{\mathrm{RTN}}^{\mathrm{J2000}} & \left.\frac{\partial \psi}{\partial \delta \boldsymbol{p}_{J2000}}\right|_{\bar{\boldsymbol{x}}}\boldsymbol{R}_{\mathrm{RTN}}^{\mathrm{J2000}}\end{pmatrix}^{\mathrm{T}}\left.\frac{\partial \delta \boldsymbol{p}_{\mathrm{RTN}}}{\partial \boldsymbol{x}}\right|_{\bar{\boldsymbol{x}}}. \tag{17}$$

The expansion given by Eq. (17) contains three main terms, namely 1) the derivative of the azimuth and elevation angles w.r.t. relative position/velocity, $\delta \boldsymbol{r}_{\mathrm{J2000}} = (\delta \boldsymbol{p}_{\mathrm{J2000}}\ \delta \boldsymbol{v}_{\mathrm{J2000}})^{\mathrm{T}}$ in the inertial frame, 2) the rotation matrix from the RTN frame to the inertial frame (see Sect. II.C), and 3) the derivatives of the relative position, $\delta \boldsymbol{p}_{\mathrm{RTN}}$, in the RTN frame w.r.t. the relative orbital elements. $\delta \boldsymbol{r}_{\mathrm{RTN}}$ represents the relative position/velocity in the RTN frame. Here usage has been made of the fact that the derivative of the angle measurements w.r.t. the relative velocity is zero. The mapping between relative orbital elements and relative position in the orbital frame is given by the adopted linear model [16, 18] as

$$\left.\frac{\partial \delta \boldsymbol{p}_{\mathrm{RTN}}}{\partial \boldsymbol{x}}\right|_{\bar{\boldsymbol{x}}}=\begin{pmatrix} 1 & -\cos u^{\mathrm{o}} & -\sin u^{\mathrm{o}} & 0 & 0 & 0 \\ 0 & 2\sin u^{\mathrm{o}} & -2\cos u^{\mathrm{o}} & 0 & \cot i^{\mathrm{o}} & 1 \\ 0 & 0 & 0 & \sin u^{\mathrm{o}} & -\cos u^{\mathrm{o}} & 0 \end{pmatrix}. \tag{18}$$

The measurements partials w.r.t. inertial relative position can be computed using the following equivalence

$$\frac{\partial \delta \boldsymbol{p}_{\mathrm{Cam}}}{\partial \delta \boldsymbol{p}_{\mathrm{J2000}}}=\boldsymbol{R}=\boldsymbol{u}^{\mathrm{c}}\frac{\partial \delta r}{\partial \delta \boldsymbol{p}_{\mathrm{J2000}}}+\delta p\frac{\partial \boldsymbol{u}^{c}}{\partial \psi}\frac{\partial \psi}{\partial \delta \boldsymbol{p}_{\mathrm{J2000}}}+\delta p\frac{\partial \boldsymbol{u}^{c}}{\partial \eta}\frac{\partial \eta}{\partial \delta \boldsymbol{p}_{\mathrm{J2000}}}, \tag{19}$$

where $\boldsymbol{R}$ represents the rotation matrix from J2000 to the camera frame (see Sect. III.B), whereas

$$\begin{aligned}\frac{\partial \boldsymbol{u}^c}{\partial \eta} &= \begin{pmatrix} \cos(\psi)\cos(\eta) \\ 0 \\ -\cos(\psi)\sin(\eta) \end{pmatrix} \\ \frac{\partial \boldsymbol{u}^c}{\partial \psi} &= \begin{pmatrix} -\sin(\psi)\sin(\eta) \\ \cos(\psi) \\ -\sin(\psi)\cos(\eta) \end{pmatrix}\end{aligned} . \tag{20}$$

Now Eq. (19) can be alternatively solved for the partials of azimuth and elevation by multiplying right and left hand sides respectively by $\left(\partial \boldsymbol{u}^c / \partial \eta\right)^{\mathrm{T}}$ and $\left(\partial \boldsymbol{u}^c / \partial \psi\right)^{\mathrm{T}}$ to produce

$$\begin{aligned}\left.\frac{\partial \eta}{\partial \delta \dot{\boldsymbol{p}}_{\mathrm{J2000}}}\right|_{\bar{x}} &= \frac{1}{\delta p \cos^2(\psi)} \left(\frac{\partial \boldsymbol{u}^{\mathrm{c}}}{\partial \eta}\right)^{\mathrm{T}} \boldsymbol{R} \\ \left.\frac{\partial \psi}{\partial \delta \dot{\boldsymbol{p}}_{\mathrm{J2000}}}\right|_{\bar{x}} &= \frac{1}{\delta p} \left(\frac{\partial \boldsymbol{u}^{\mathrm{c}}}{\partial \psi}\right)^{\mathrm{T}} \boldsymbol{R}\end{aligned} . \tag{21}$$

At this stage all the ingredients are available to go back to Eq. (17) and compute the sensitivity matrix $\boldsymbol{C}$(t).

The least-squares relative orbit determination aims at finding the state $\boldsymbol{x}^{\mathrm{lsq}}(t_{\mathrm{n}}) = \boldsymbol{x}^{\mathrm{lsq}}$ that minimizes the weighted squared sum of the difference between the modeled observations $\boldsymbol{y}_i$ and the actual measurements $\boldsymbol{z}_i$ [c.f., Eq. (12, 13)]. Here the 2D vector measurements of the batch are indexed through $i = (1,\ldots,n)$, where n represents the number of processed images taken at times $t_1,\ldots,t_n$. Since the full state can not be reconstructed from a set of angles-only measurements, a-priori information $\boldsymbol{x}^{\mathrm{apr}}$ other than the available measurements is necessary to initialize the filter. If information on the accuracy of this value is available, the a-priori covariance $\boldsymbol{P}^{\mathrm{apr}}$ of the state can be incorporated into the least-squares estimation which aims at minimizing the following performance index

$$J(\boldsymbol{x}) = (\tilde{\boldsymbol{z}} - \tilde{\boldsymbol{c}})^{\mathrm{T}} (\tilde{\boldsymbol{z}} - \tilde{\boldsymbol{c}}) + (\boldsymbol{x} - \boldsymbol{x}^{\mathrm{apr}})^{\mathrm{T}} \left(\boldsymbol{P}^{\mathrm{apr}}\right)^{-1} (\boldsymbol{x} - \boldsymbol{x}^{\mathrm{apr}}) = \boldsymbol{\rho}^{\mathrm{T}} \boldsymbol{\rho} + (\boldsymbol{x} - \boldsymbol{x}^{\mathrm{apr}})^{\mathrm{T}} \boldsymbol{\Lambda}^{\mathrm{apr}} (\boldsymbol{x} - \boldsymbol{x}^{\mathrm{apr}}) , \tag{22}$$

where $\boldsymbol{\Lambda} = \boldsymbol{P}^{-1}$ is also known as the information matrix, and $\boldsymbol{\rho}$ represents the measurement residuals [21]. These are accumulated over the complete batch as follows

$$\boldsymbol{\rho}^{\mathrm{T}} = \left(\tilde{\boldsymbol{z}} - \tilde{\boldsymbol{c}}\right)^{\mathrm{T}} = \begin{pmatrix} \boldsymbol{z}_1 - \boldsymbol{c}_1(\boldsymbol{x}_1) & \cdots & \boldsymbol{z}_n - \boldsymbol{c}_n(\boldsymbol{x}_n) \end{pmatrix}, \tag{23}$$

where $\boldsymbol{c}_{\mathrm{i}} = \boldsymbol{c}(\boldsymbol{x}_{\mathrm{i}})$ is given by Eq. (12) as a non-linear function of the relative position, and $\boldsymbol{x}_{\mathrm{i}} = \boldsymbol{x}(t_{\mathrm{i}})$ is computed using the first of Eq. (13) which includes eventual orbit control maneuvers occurred in the data arc. It is noted that since the filter is initialized at the final time, t_{n}, of the batch, the propagation of the state is done backward in time while processing measurements which are subsequently older (i.e., $t_{\mathrm{n}} > t_{\mathrm{n-1}} > \ldots > t_1$). This is compatible with Eqs. (15, 16) as long as the sign of $\Delta t = t_{i-1} - t_i$ is properly retained in the computations. The relative state which best fits the observations in a least-squares of the residuals sense, or in other words, which minimizes the loss function defined by Eq. (22), is given by the iterations

$$\begin{aligned}\boldsymbol{x}_{j+1}^{\mathrm{lsq}} &= \boldsymbol{x}_j^{\mathrm{lsq}} + (\boldsymbol{\Lambda}^{\mathrm{apr}} + \tilde{\boldsymbol{C}}_j^{\mathrm{T}} \tilde{\boldsymbol{W}}^{-1} \tilde{\boldsymbol{C}}_j)^{-1} [\boldsymbol{\Lambda}^{\mathrm{apr}} (\boldsymbol{x}_j^{\mathrm{lsq}} - \boldsymbol{x}^{\mathrm{apr}}) + \tilde{\boldsymbol{C}}_j^{\mathrm{T}} \tilde{\boldsymbol{W}}^{-1} \boldsymbol{\rho}_j] \\ \boldsymbol{P}_{j+1}^{\mathrm{lsq}} &= (\boldsymbol{\Lambda}^{\mathrm{apr}} + \tilde{\boldsymbol{C}}_j^{\mathrm{T}} \tilde{\boldsymbol{W}}^{-1} \tilde{\boldsymbol{C}}_j)^{-1}\end{aligned} , \tag{24}$$

which are started from $\boldsymbol{x}_0^{\mathrm{lsq}} = \boldsymbol{x}^{\mathrm{apr}}$ and continued until convergence, typically after 4-5 iterations. Here the weighting matrix $\tilde{\boldsymbol{W}} = \mathrm{diag}(\boldsymbol{W}_1,\ldots,\boldsymbol{W}_{\mathrm{n}})$ is introduced for generality to show how different accuracies of the angle measurements

can be easily accounted for within the same batch, for example as a function of the separation to target. In the following, for simplicity, the measurement a-priori standard deviation has been taken to be constant, i.e. $\boldsymbol{W}_i = \boldsymbol{W}$ for all collected images. A basic data editing approach is implemented in ROD to discard measurements which are obviously wrong. The editing criterion is based on the root mean square (rms) of the residuals which are expected to stay below a user defined threshold. Throughout the five-day ARGON experiment, the a-priori state $\boldsymbol{x}^{\text{apr}}$ and its covariance $\boldsymbol{P}^{\text{apr}}$ are inherited from the previous run of ROD. This requires a propagation step from the end-time of the previous batch to the new end-time t_n which is normally in the forward direction. Only at the beginning of the experiment, since no camera images were available, the a-priori information was derived from the combination of GPS precise orbit determination of the servicer spacecraft and NORAD TLE orbit determination of the client (see Sect. III.E).

D. Maneuver Planning and Commanding (MAP)

Given the latest estimate of the relative orbital elements, $\boldsymbol{x}^{\text{lsq}}$, provided by ROD at time t_n, MAP aims at computing the necessary orbit correction maneuvers to acquire (or maintain) a desired formation configuration, $\boldsymbol{x}^{\text{des}}$, at some future time t. The corresponding maneuver planning problem can be solved analytically under the assumptions of the linear relative motion model (i.e., $J_2 << 1$, $e << 1$, $\delta r/a^o << 1$). In particular the first of Eq. (13) can be solved for the unknown impulsive delta-v maneuver $\Delta\boldsymbol{v}$ and its application time t_M as follows

$$\Delta\boldsymbol{v}(t_M) = \boldsymbol{B}(t,t_M)^{-1}[\boldsymbol{x}(t) - \boldsymbol{\Phi}(t,t_M)\boldsymbol{x}(t_M)] = \boldsymbol{B}(t,t_M)^{-1}[\boldsymbol{x}^{\text{des}} - \boldsymbol{\Phi}(t,t_n)\boldsymbol{x}^{\text{lsq}}] = \boldsymbol{B}^{-1}\Delta\boldsymbol{x}^{des}, \tag{25}$$

where $\boldsymbol{\Phi}$ and $\boldsymbol{B}$ are given by Eqs. (15, 16) and the operator $\Delta(\cdot)$ represents the difference between the desired and estimated relative orbital elements (propagated at the same time t). For a single pulse, Eq. (25) corresponds to an overdetermined system with 4 unknowns and 6 linearly independent equations, i.e. the inverse of $\boldsymbol{B}$ does not exist. This case yields no solution or, in other words, one single maneuver is not able to provide an arbitrary correction of all relative orbital elements. Necessarily multiple pulses have to be introduced to solve the problem. First of all we take advantage of the decoupling between in-plane and out-of-plane motion. The partition of Eq. (25) which governs the evolution of the relative inclination vector is characterized by 2 linearly independent equations which can be solved for the 2 unknowns, Δv_N and $u_M(t_M)$, as

$$\begin{cases} \Delta v_N = n^o a^o \Delta\delta i^{\text{des}} \\ u_M = \text{atan}(\Delta\delta i_y^{\text{des}} / \Delta\delta i_x^{\text{des}}) \end{cases}, \tag{26}$$

where u_M identifies the mean argument of latitude of the servicer at the delta-v time. If the maneuver size exceeds a user-defined threshold, the out-of-plane maneuver planning splits Eq. (26) in two impulses of individual size $\Delta v_N/2$ separated by half an orbital revolution.

Since the partition of Eq. (25) which governs the evolution of the in-plane motion (i.e., δa, $\delta\boldsymbol{e}$, and δu) is still overdetermined, a double-impulse approach is adopted which gives 4 equations in the 6 unknowns Δv_{Ri}, Δv_{Ti} and u_{Mi} with i=1,2. Of the infinite available solutions, the following two sets have been chosen for the implementation of ARGON, motivated by arguments of simplicity, fuel-efficiency, and observability. The first set corresponds to maneuvers in the along-track direction separated by half an orbit [18]

$$\begin{cases} \Delta v_{T1} = n^o a^o (\Delta\delta a^{\text{des}} + \Delta\delta \text{e}^{\text{des}})/4 \quad \text{at} \quad u_{M1} = \arctan(\Delta\delta e_y^{\text{des}} / \Delta\delta e_x^{\text{des}}) \\ \Delta v_{T2} = n^o a^o (\Delta\delta a^{\text{des}} - \Delta\delta \text{e}^{\text{des}})/4 \quad \text{at} \quad u_{M2} = u_{M1} + \pi \end{cases}, \tag{27}$$

whereas the second set results from a combination of along-track and radial maneuvers as follows [18]

$$\begin{cases} \Delta v_{T1} = n^o a^o \Delta\delta a^{\text{des}}/4, \quad \Delta v_{R1} = n^o a^o \Delta\delta e^{\text{des}}/2 \quad \text{at} \quad u_{M1} = \arctan(\Delta\delta e_x^{\text{des}} / \Delta\delta e_y^{\text{des}}) \\ \Delta v_{T2} = n^o a^o \Delta\delta a^{\text{des}}/4, \quad \Delta v_{R2} = -n^o a^o \Delta\delta e^{\text{des}}/2 \quad \text{at} \quad u_{M2} = u_{M1} + \pi \end{cases}. \tag{28}$$

The first difference between Eq. (27) and (28) lies in the way the relative eccentricity vector is controlled, i.e., via along-track or radial maneuvers respectively. The use of Eq. (27) is normally preferred due to the reduced delta-v consumption; in fact along-track maneuvers have double efficiency with this respect [see factor 2 in terms related to the along-track maneuvers in the matrix $\boldsymbol{B}$, Eq. (16)]. On the other hand, especially for closer separations, radial maneuvers are shown to be more beneficial from an observability point of view, since they induce instantaneous variations of the range [34]. In contrast to the real-time on-board implementation of this control method described in [5], here the orbit corrections are computed on-ground by MAP before the execution of the pair of maneuvers on-board. Since no ground-contacts are normally available in between the maneuvers of the same pair, no navigation data can be used to refine the plan and compensate eventual execution errors. Inevitably, these will accumulate until the execution of the next maneuver pair.

A second important difference between Eq. (27) and (28) is that only the latter is able to acquire an arbitrary set of desired relative orbital elements (i.e., δa^{des}, $\delta \boldsymbol{e}^{\mathrm{des}}$, and δu^{des}) at time $t = t_2$ (i.e., right after the execution of the maneuver pair). This is due to the fact that Eq. (27) offers only 4 degrees of freedom against 6 equations. Despite this apparent limitation, the along-track approach with double-burns is still viable and preferred here to triple-burns because of its simplicity. Since the rendezvous strategy foresees regular maneuvers planned and executed in a step-wise fashion for better observability, $\delta \boldsymbol{e}^{\mathrm{des}}$ is usually prescribed at time t_2, whereas the desired mean along-track separation $\delta\lambda^{\mathrm{des}}$ can be set to be acquired at a later time t_{f} which corresponds to the start time of the next pair of in-plane maneuvers (i.e., the next t_1). The necessary correction of the relative semi-major axis $\Delta\delta a^{\mathrm{des}}$ to be established by the maneuver pair is then computed by [16,18]

$$\Delta\delta a^{\mathrm{des}} = \delta a^{\mathrm{des}} - \delta a_{\mathrm{M1}} = -\frac{2}{3}\frac{\Delta\delta\lambda^{\mathrm{des}}}{u_{\mathrm{f}}^{\mathrm{o}} - u_{\mathrm{M1}}^{\mathrm{o}}} - \delta a_{\mathrm{M1}} = \frac{-2/3\,(\delta\lambda_{\mathrm{f}}^{\mathrm{des}} - \delta\lambda_{\mathrm{M1}}) - \Delta\delta e^{\mathrm{des}}\,\pi/2 - (u_{\mathrm{f}}^{\mathrm{o}} - u_{\mathrm{M1}}^{\mathrm{o}} - \pi)\delta a_{\mathrm{M1}}}{u_{\mathrm{f}}^{\mathrm{o}} - u_{\mathrm{M1}}^{\mathrm{o}} + \pi/2}, \tag{29}$$

for along-track maneuvers [i.e., with Eq. (27)], and by

$$\Delta\delta a^{\mathrm{des}} = \delta a^{\mathrm{des}} - \delta a^{\mathrm{lsq}} = -\frac{2}{3}\frac{\Delta\delta\lambda^{\mathrm{des}}}{u_{\mathrm{f}}^{\mathrm{o}} - u_{\mathrm{M1}}^{\mathrm{o}}} - \delta a^{\mathrm{lsq}} = \frac{-2/3\,(\delta\lambda_{\mathrm{f}}^{\mathrm{des}} - \delta\lambda_{\mathrm{M1}}) - (u_{\mathrm{f}}^{\mathrm{o}} - u_{\mathrm{M1}}^{\mathrm{o}} - \pi)\delta a^{\mathrm{lsq}}}{u_{\mathrm{f}}^{\mathrm{o}} - u_{\mathrm{M1}}^{\mathrm{o}} + \pi/2}, \tag{30}$$

if a combination of along-track and radial maneuvers is adopted [i.e., with Eq. (28)]. Here the subscript M1 identifies quantities at the time of the first maneuver, t_{M1}, which are all known during the current maneuver planning session (i.e., resulting from propagation of ROD and POD outputs). As discussed in the next chapter, typically two maneuver planning sessions are done per day. Each session delivers a maximum of four time-tagged maneuvers (i.e., 2 in-plane and 2 out-of-plane) which are executed during dedicated delta-v slots in the experiment time schedule. For each maneuver computed by MAP a corresponding command file in the standard Procedure Language for Users in Test and Operations (PLUTO) [35] is generated for upload to the spacecraft during the subsequent uplink ground-contact.

E. Precise Orbit Determination (POD) and Two Line Elements (TLE)

The ARGON flight dynamics system requires an estimate of the absolute state of the servicer (c.f., ROD and MAP in Fig. 4) and of the executed orbit control maneuvers (c.f., ROD in Fig. 4). To this end, use is made of the PRISMA POD facility [15] which is based on the DLR's in-house GPS High precision Orbit determination Software Tools (GHOST) [32]. This software suite is already used routinely to support many missions at GSOC and has already proved its high readiness level as well as its ability to provide reliable and accurate orbit products. The data processing for precise orbit determination follows a step-wise scheme. First the raw GPS pseudorange and carrier-phase measurements are processed to derive a kinematic single-point-positioning navigation solution. The measurements which are obviously corrupted are discarded according to the values of the rms of the residuals. The resulting set of discrete navigation points is affected by errors at the meter level. For single-frequency receivers a bias of several meters due to the ionosphere can be observed in the radial direction (such as on PRISMA). Second, this kinematic solution is filtered dynamically using a batch least-squares process, which relies on accurate models of the spacecraft dynamics. This orbit solution is continuous and slightly more accurate than the purely kinematic positioning, being affected by a much smaller radial bias. Third, a precise orbit determination is done using the previously computed coarse orbit solution for rigorous data editing based on measurements residuals. This program is a weighted batch least-squares processor with a-priori information which processes GRAPHIC measurements

[36]. The output estimates include the state of the spacecraft, the delta-v maneuvers, as well as other force and measurement model parameters such as drag coefficient, solar radiation pressure coefficient, carrier phase biases and empirical accelerations. These orbit products are characterized by a positioning accuracy better than 50 cm (3D, rms) [37] and are accompanied by delta-v maneuver estimates which are up to 10% more accurate than the a-priori information based on the commanded thruster burn times. Precise knowledge of the executed delta-v maneuvers is required for angles-only navigation because of the known lack of observability [17].

Within ARGON, the Tango client satellite is treated as a non-cooperative object, e.g., an eventual customer in an on-orbit-servicing scenario. Therefore, despite their availability, no GPS data of the client can be used during the experiment execution. One of the goals of ARGON was to mimic a lost-in-space situation before the activation of the VBS FAR camera. Thus, in order to derive a meaningful knowledge of the formation relative motion, a combination of POD products of Mango and NORAD TLEs of Tango has been used. Such a strategy has basically no cost, since TLE sets are made publicly available on a regular basis in a standardized format for use with the Simplified General Perturbations (SGP) orbital models [38]. On the other hand, TLEs have no widely accepted propagation accuracy metrics. Thus a preliminary analysis was deemed necessary to understand the expected relative navigation errors at experiment start. This was performed through the use of PRISMA flight data collected on March 17-18, April 5-6, and August 20-21, 2011. The corresponding TLEs of Tango have been propagated using the SGP-4 orbit model over a time frame of 48 hours and compared with Tango GPS POD ephemeris covering the same arc. The statistics of the orbit propagation error are provided in Table 2 for each relative orbital element (c.f., Unfiltered TLEs). The results show standard deviations of the order of 500 m in the relative mean argument of latitude and 100 m in the remaining relative orbital elements. These errors, coupled with the large error in relative semi-major axis, motivated the need to further process the SGP-4 propagated states as pseudo-measurements in a reduced dynamic batch least-squares orbit determination. The resulting statistics are also listed in Table 2 (c.f., Filtered TLEs), which show standard deviations better by one to two orders of magnitude and similar mean errors as compared to the unfiltered approach. On one hand, this strategy is shown to be satisfactory for a first estimation of the mean along-track separation and its drift. This provides enough confidence in the establishment of a first safe separation between the satellites in the along-track direction. On the other hand, the relative eccentricity and inclination vectors are affected by offsets of the order of hundreds of meters. This makes TLEs of the client spacecraft unreliable if used to establish a relative eccentricity/inclination vector separation.

Table 2. Relative navigation errors based on client TLEs and servicer GPS POD orbits.

Relative orbital elements	Unfiltered TLEs		Filtered TLEs	
Statistics over 48 hours	Abs(mean) [m]	Std [m]	Abs(mean) [m]	Std [m]
$E(a\delta a)$	2.5	79.1	2.0	1.3
$E(a\delta e_x)$	49.3	122.7	158.0	2.3
$E(a\delta e_y)$	25.3	78.2	30.0	1.3
$E(a\delta i_x)$	50.5	165.6	46.5	0.6
$E(a\delta i_y)$	565.7	99.2	432.1	0.9
$E(a\delta u)$	938.0	466.2	726.9	80.6

IV. EXPERIMENT PLAN

This section provides an overview of the ARGON operations concept and of the rendezvous guidance approach. In particular the key design items which have driven the selection of the experiment initial and final conditions are discussed.

A. Operations Concept

The ARGON experiment operations concept includes three major elements, namely the PRISMA Mission Control Center (MCC), the Experiment Control Center (ECC), both located at Stockholm/Solna, and the ESRANGE/Kiruna ground-station. The MCC is under OHB-SE management and has the responsibilities of overall mission control, including procedure validation, commanding, telemetry pre-processing, spacecraft bus operations and health monitoring among others. The ECC is under DLR/GSOC management and has the overall experiment responsibility, including the operations of the ARGON flight dynamics system described in the previous section. The MCC constitutes the ultimate in/out interface between the spacecraft and the ECC. In addition, it was responsible for the acquisition of the formation initial conditions. These were prescribed by ECC in terms of nominal relative orbital elements and associated errors induced by TLE navigation (see Table 2).

The ESRANGE/Kiruna ground-station was used during ARGON to establish uplink and downlink communication with the spacecraft. In combination with the 720/780 km altitude sun-synchronous orbit with 98.28° inclination, this gave approximately 10 passages per day of about 10 minutes duration each. The typical passage schedule is illustrated in Fig. 5, including the main involved activities. For most of the day, all relevant telemetry data (e.g., attitude, GPS and VBS FAR) which are stored in the servicer mass-memory during one orbital revolution (about 100 min.) can be downloaded at the subsequent ground-contact (see Fig. 5, TM Download). An exception is made between 05:00 and 14:00 UTC each day, where Mango is not visible from Kiruna. A dedicated strategy has been studied to guarantee the timely availability of TM with no delays and, at the same time, minimize the loss of data. In particular the TM configuration was set to a lower data-rate during this time frame. At the first contact of the day (ca. 14:00 UTC), the mass-memory pointer was reset in such a way that the most recent data, covering the last 2-hour arc, were downloaded. This approach was robust enough for routine operations and provided a total of approximately 7-hour long data gaps each day (i.e., btw. 05:00 and 12:00 UTC).

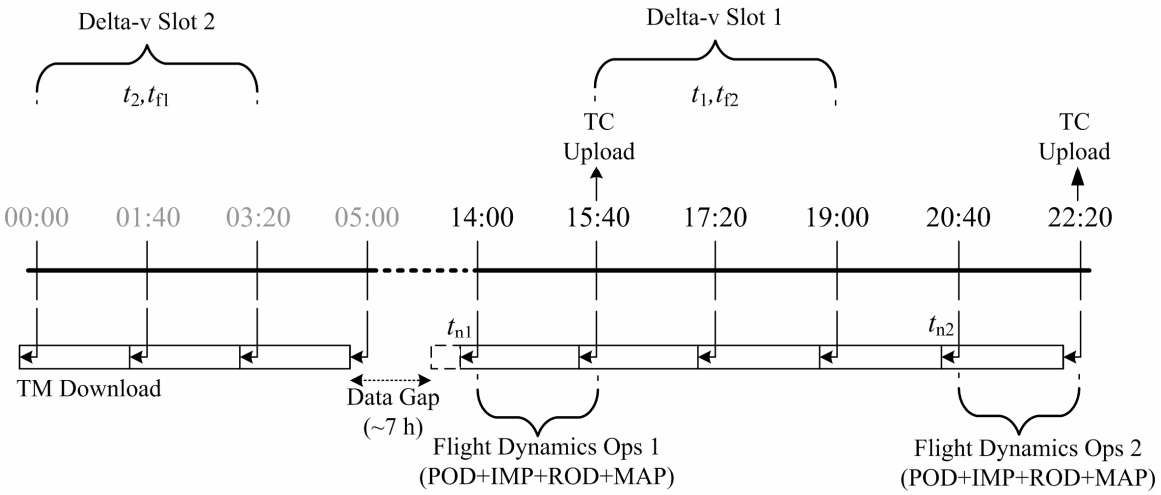

Figure 5. ARGON baseline operational day highlighting key on-ground (bottom half) and on-board activities (top half). The ground-contacts (~10/day) are tagged with the approximate time (UTC) of signal acquisition. The unmanned ground passages are indicated with gray time-tags.

Fig. 5 indicates the main use of the available ground-passages. The unmanned contacts between 00:00 and 14:00 UTC were only used for TM dumps, whereas the manned contacts between 14:00 and 22:20 UTC were used for monitoring and TC uploads. The core ECC flight dynamics operations were concentrated in two time slots (see Fig. 5, Flight Dynamics Ops 1 and 2) between two subsequent passages over Kiruna (i.e., 14:00-15:40 and 20:40-22:20 UTC). Each operations slot gave the possibility to process the latest income TM through the complete chain of software modules described in the previous section (i.e., POD, IMP, ROD, MAP) and finally generate the maneuver TCs for upload to the spacecraft by the MCC (typically at 15:40 and 22:20 UTC). In order to minimize the elapsed time between the state estimates of ROD at t_{ni} (i.e., latest available VBS FAR image data) and maneuver times for formation acquisition/keeping at t_i, two delta-v slots have been defined right after and in close vicinity of the planning sessions (see Fig. 5, Delta-v Slot 1 and 2). Representative time tags for t_{ni} and t_i are also provided in Fig. 5, where i=1,2 represents the associated flight dynamics operations slot. In order to properly estimate the executed orbit control maneuvers (by POD) for incorporation in the angles-only relative orbit determination process (by ROD), care was taken to ensure the presence of TM data during maneuver-free periods for at least one orbit before and after the delta-v slots.

The ARGON operations timeline during the first day of experiment execution differs substantially from days 2 to 5. This is due to two main reasons. First of all, the experiment started on the first passage of the day around 14:00 UTC on April 23, 2012. The morning earlier hours were used to setup the ECC in Stockholm/Solna. Secondly, the VBS FAR camera was switched on at experiment start only, so that the first dump of VBS FAR data occurred at the second contact of the day. As a consequence, the very first flight dynamics operations slot did not involve any image processing (IMP) or angles-only relative navigation (ROD), but was rather dedicated to maneuver planning (MAP)

based on GPS precise orbit determination of the servicer (POD) and TLE orbit determination of the client (TLE). In view of the expected poor TLE navigation accuracy, these maneuvers were only intended to improve the observability of the system for the subsequent ROD sessions.

B. Rendezvous Guidance Profile

As discussed above, the ARGON operations concept foresees a total of 9 delta-v slots (i.e., 1 delta-v slot for the first day and 2 delta-v slots per experiment day 2 to 5). For each delta-v slot a desired formation configuration has to be defined, which MAP tries to acquire according to the algorithms presented in Sect. III.D. The overall set of aimed relative orbital elements throughout ARGON is referred to as the guidance profile in the following.

The guidance profile follows a strategy based on the relative eccentricity/inclination vector separation method. The goal is to first acquire an anti-parallel configuration of $\delta\boldsymbol{e}$ and $\delta\boldsymbol{i}$, and then reduce the magnitude of these vectors in a step-wise manner. In parallel, the relative mean argument of latitude (or mean along-track separation) is reduced through step-wise corrections of the relative semi-major axis. The finally aimed formation configuration corresponds to a delivery geometry with zero along-track drift (or zero relative semi-major axis). This results in a typical helix motion with shrinking radius as described in [39]. On one hand, the relative navigation errors are expected to be larger at experiment start because of the reduced observability (and initial TLE navigation errors). On the other hand, the visibility and safety constraints as well as the control accuracy objectives have more weight at experiment end, close to the delivery time. These aspects drive the selection of a guidance profile characterized by changes of the relative orbital elements which are gradually increased from a minimum at experiment start to a maximum halfway through the experiment. Conversely, the relative orbit corrections are gradually decreased from their maximum at experiment half to their minimum at experiment end. In order to mitigate the accumulation of control errors due to the ground-based operations, the morning delta-v slot of each day (see Fig. 5, Delta-v Slot 2) is used to implement the desired changes of the relative eccentricity and inclination vectors (i.e., acquisition), whereas the afternoon delta-v slot of each day (see Fig. 5, Delta-v Slot 1) is used for fine tuning and maintenance.

Given the aforementioned guidelines for the selection of the guidance profile, two main unknowns remain, namely the initial and final formation configurations. The initial nominal formation geometry to be acquired by the MCC was chosen at 30 km mean along-track separation ($a^{o}\delta\lambda$ = -30 km), with no along-tack drift rate ($a^{o}\delta a$ = 0), and amplitudes of the radial and cross-track oscillations of 400 m ($a^{o}\delta i_y = -a^{o}\delta e_y$ = 400 m, $a^{o}\delta e_x = -a^{o}\delta i_x$ = 0). The selected relative orbital elements ensure visibility of the client spacecraft in the presence of TLE uncertainties (see Table 2), furthermore the size of the nominal relative eccentricity and inclination vectors is of the same order of magnitude of the expected TLE errors. The final aimed formation geometry results instead from a trade-off which takes into account the visibility and safety constraints defined in Sect. II.C. In particular, Eqs. (3,5) can be extended to take into account the control uncertainties which affect the relative orbital elements as follows

$$\begin{cases} \tan(\alpha_{\max})|\delta\lambda| - |\delta e + \delta a^*| \geq 3|\delta\lambda|\sigma[(\delta e + \delta a^*)/\delta\lambda] = 3\left\{\delta\lambda^2\sigma^2[(\delta e + \delta a^*)/\delta\lambda]\right\}^{0.5} \\ \tan(\beta_{\max})|\delta\lambda| - \delta i \geq 3|\delta\lambda|\sigma[\delta i/\delta\lambda] = 3\left\{\delta\lambda^2\sigma^2[\delta i/\delta\lambda]\right\}^{0.5} \\ \delta r_{\mathrm{RNmin}} - \mathrm{M} \geq 3\sigma[\delta r_{\mathrm{RNmin}}] = 3\left\{\sigma^2[\delta r_{\mathrm{RNmin}}]\right\}^{0.5} \end{cases}, \tag{31}$$

where the operator $\sigma[\cdot]$ represents the standard deviation of its argument. Under the assumption of unbiased, uncorrelated state errors, the combined standard uncertainty can be expressed as follows

$$\begin{cases} \delta\lambda^2\sigma^2[(\delta e + \delta a^*)/\delta\lambda] = \sigma^2[\delta e] + \sigma^2[\delta a^*] + \sigma^2[\delta\lambda](\delta e + \delta a^*)^2/\delta\lambda^2 \\ \delta\lambda^2\sigma^2[\delta i/\delta\lambda] = \sigma^2[\delta i] + \sigma^2[\delta\lambda]\delta i^2/\delta\lambda^2 \\ \sigma^2[\delta r_{\mathrm{RNmin}}] = \left\{\sigma^2[\delta i], \sigma^2[\delta e] + \sigma^2[\delta a^*]\right\} \end{cases}. \tag{32}$$

The single standard deviations of the relative orbital elements can be derived from the first of Eq. (13) as a combination of navigation and maneuver execution errors

$$\begin{cases} \sigma^2[\delta a^*] = \sigma^2_{\text{nav}}[\delta a] + \sigma^2_{\text{nav}}[\delta\lambda]/\delta\lambda^2 + 4\sigma^2_{\text{man}}[\Delta v_{\text{T}}]/(a^{\text{o}}n^o)^2 \\ \sigma^2[\delta e] = \sigma^2_{\text{nav}}[\delta e] + 4\sigma^2_{\text{man}}[\Delta v_{\text{T}}]/(a^{\text{o}}n^o)^2 \\ \sigma^2[\delta i] = \sigma^2_{\text{nav}}[\delta i] + \sigma^2_{\text{man}}[\Delta v_{\text{N}}]/(a^{\text{o}}n^o)^2 \\ \sigma^2[\delta\lambda] = \sigma^2_{\text{nav}}[\delta\lambda] + 1.5\Delta t^2_{\text{man}}\sigma^2_{\text{nav}}[\delta a]n^{\text{o}2} + 9\Delta t^2_{\text{man}}\sigma^2_{\text{man}}[\Delta v_{\text{T}}]/a^{o2} \end{cases}, \tag{33}$$

where single burns are assumed in along-track and cross-track directions, $\Delta t_{\text{man}} = t_{\text{f}} - t_{\text{n}}$ represents the maneuver planning delay, and Earth oblateness effects are neglected for short time propagations (i.e., $\Delta t_{\text{man}} \le 24$ hours).

Table 3. Key parameters selected for simplified propagation of state uncertainty.

Item	Unit	Value
$\alpha_{\max}$ (c.f., Table 1)	deg	9.15
$\beta_{\max}$ (c.f., Table 1)	deg	6.85
$\sigma_{\text{nav}}[a^{\text{o}}\delta e, a^{\text{o}}\delta i]$	m	30
$\sigma_{\text{nav}}[a^{\text{o}}\delta a]$	m	5
$\sigma_{\text{nav}}[a^{\text{o}}\delta\lambda]$	m	300
$\sigma_{\text{man}}[\Delta v_{\text{T}}, \Delta v_{\text{N}}]$	mm/s	1
Δt_{man}	h	24
M	m	20

The back substitution of Eq. (33) and Eq. (32) into Eq. (31), gives an expression of the ARGON constraints as an implicit function of the control uncertainties on δa, δe, δi, $\delta\lambda$ [here denoted as $\delta(\cdot)$] which has the following structural form

$$\begin{cases} C[\alpha_{\max}, \delta(\cdot)] \ge C\{\sigma_{\text{nav}}[\delta(\cdot)], \sigma_{\text{man}}[\Delta v_{\text{T}}], \Delta t_{\text{man}}, \delta(\cdot)\}_{\text{err}} \\ C[\beta_{\max}, \delta(\cdot)] \ge C\{\sigma_{\text{nav}}[\delta(\cdot)], \sigma_{\text{man}}[\Delta v_{\text{N}}], \Delta t_{\text{man}}, \delta(\cdot)\}_{\text{err}} \\ C[\text{M}, \delta(\cdot)] \ge C\{\sigma_{\text{nav}}[\delta(\cdot)], \sigma_{\text{man}}[\Delta v_{\text{T}}, \Delta v_{\text{T}}], \Delta t_{\text{man}}, \delta(\cdot)\}_{\text{err}} \end{cases}. \tag{34}$$

Eq. (34) is valid for (anti-)parallel relative eccentricity/inclination vectors.

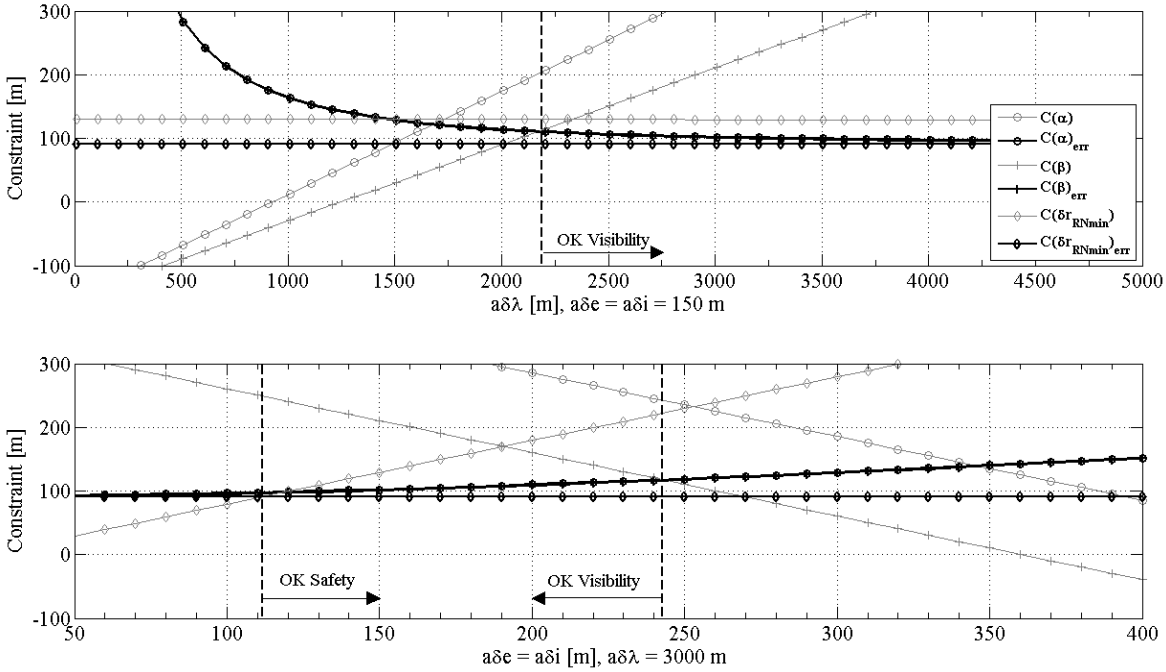

Figure 6. ARGON visibility and safety constraints evaluated at trade-off delivery point.

Given the values listed in Table 3 for the parameters α_{max}, β_{max}, σ_{nav}, σ_{man}, Δt_{man}, and M, a trade-off choice for the final formation configuration of $a^o\delta e = a^o\delta i = 150$ m and $a^o\delta\lambda = -3$ km has been made. The resulting margins of this solution with respect to the constraint errors are illustrated in Fig. 6. The top subplot shows the evolution of the constraints with constant $\delta e = \delta i$ and independent $\delta\lambda$, whereas the bottom subplot shows the evolution of the constraints with constant $\delta\lambda$ and varying $\delta e = \delta i$. The dashed vertical lines represent the boundaries where Eq. (34) is satisfied as equality, whereas the constraints are not satisfied as soon as the gray lines result smaller than the corresponding black lines (i.e., $C < C_{err}$). Given the above mentioned choice of the final formation and in the presence of uncertainties, client visibility can be guaranteed for mean along-track separations above 2200 m and maximum radial/cross-track oscillation amplitudes of 240 m. The safety constraint is satisfied for $\delta e = \delta i \geq 110$ m. In other words, the selected aimed formation provides safety and visibility even if on top of the expected control uncertainties (see Table 3), additional errors occur which cause a reduction of 800 m in $\delta\lambda$ and 40 m in δe or δi. These margins make the selected final formation quite conservative, especially considering that the applied maneuver planning delay of 24 hours takes into account eventual contingencies which force the skipping of one delta-v slot in the operational schedule.

V. FLIGHT RESULTS

This section provides flight results from the execution of ARGON during the extended phase of the PRISMA mission in April 2012. After an overview of the operations activities, a performance assessment of the sensor, navigation, and control functions is presented. To this end, precise GPS relative orbit products accurate at the decimeter level [15,4] are used which have been generated post-facto after the experiment execution.

A. Overview

Upon conclusion of the preparation activities, the ARGON flight experiment started on April 23, 2012 - 14:21 UTC with the PRISMA orbit number 9764 (ca. 650 days from launch). For the first time during the mission, a team of experimenters was not aware of the actual initial conditions of the formation and did not have access to the relative GPS data which have always been used as reference. During the first contact, the VBS sensor was switched on. Immediately after, the freshly received servicer GPS and attitude data and the daily NORAD TLEs of the client have been used to determine a coarse estimate of the relative orbit of Tango w.r.t. Mango (see Sect. III.E). The formation geometry was found to be several hundreds of meters off the nominal values in the relative eccentricity and inclination vectors, with a Mango mean along-track separation of 30 km ahead of Tango and a residual drift of ca. 25 m/orbit in the anti-velocity direction. For completeness TLE-based estimates and nominal values are listed in Table 4. In addition, the obtained error as compared with the post-facto GPS POD is provided. Note that these errors were not known during ARGON.

Table 4. Relative orbital elements estimated from client TLEs at ARGON start (13:00 UTC).

Parameter [m]	TLE-based Estimates	Error (Estimate - POD Reference)	Nominal (desired)
$a^o\delta a$	-2.18	1.53	0
$a^o\delta e_x$	-218.52	112.72	0
$a^o\delta e_y$	-527.21	132.29	-400
$a^o\delta i_x$	-14.57	12.92	0
$a^o\delta i_y$	-448.99	651.01	400
$a^o\delta\lambda$	-30012.91	-47.57	-30000

Within one hour after the first contact, the experimenter team was able to execute the planned sequence of ECC orbit determination and maneuver planning tasks (i.e., modules POD, TLE, and MAP in Figure 4) and deliver to MCC the desired maneuver commands for upload during the second passage at 16:00 UTC. This passage provided the possibility to download the first orbit of VBS FAR ROIs and three JPEG images (the very first one is shown in Fig. 2 - top/right). The handover from NORAD TLEs to vision-based navigation was smoothly performed within the successive three orbits, once a sufficient number of camera measurements was available for angles-only relative orbit determination around the executed orbit control maneuvers (i.e., module ROD in Figure 4). Despite the availability of camera ROIs at about once every 2 s, the ARGON flight dynamics system made use of these image portions every ca. 30 s in order to demonstrate the capability to rely on a reduced amount of measurements. As foreseen by the ARGON operational concept two flight dynamics sessions were performed each day. These resulted in the execution of sequences of in-plane and out-of-plane maneuvers in the afternoon and early morning (see Fig. 5,

Delta-v Slot 1 and 2) to perform the desired rendezvous and, at the same time, improve the accuracy of the range estimate. The daily early maneuvers were intended to reconfigure the formation geometry, whereas the afternoon ones were planned for formation keeping after compensation of the residual navigation and control errors.

A comparison of the ROD state estimates obtained during the experiment with the GPS POD products has been done after the conclusion of ARGON as illustrated in Fig. 7. Here the difference between estimated and reference states is computed at the end time of each measurement batch processed by ROD (i.e., the state estimation time, t_{ni}). Since this state is used by MAP for maneuver planning, its accuracy drives the formation acquisition and keeping performance. The results demonstrate navigation errors which are similar to the ones obtained by the rehearsal tests conducted during the preparation activities [17]. For most of the ROD runs (i.e., 8 out of 10), the maximum errors of the estimated relative orbital elements are ±3 m in the relative semi-major axis, ±10 m in the magnitude of the relative eccentricity/inclination vectors, and ±400 m in the mean along-track separation (i.e., about 1% of the initial along-track separation). The overall trend of the relative navigation accuracy indicates a nearly constant behavior with some marginal improvements for smaller separations, especially in δa, δe_x and δi_x.

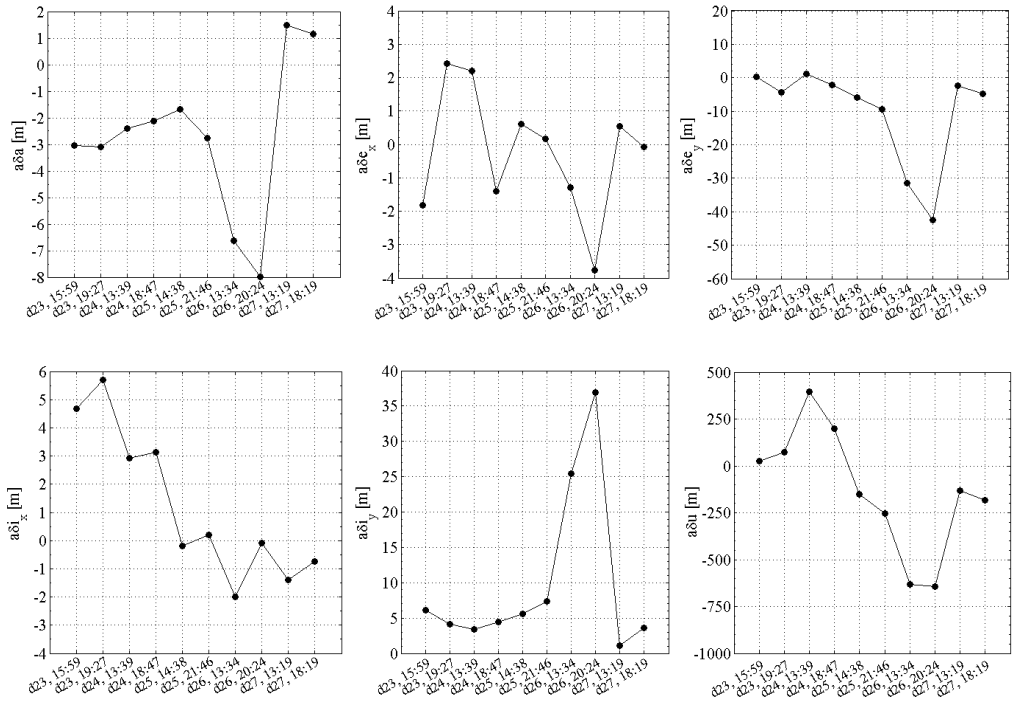

Figure 7. Angles-only relative orbit determination errors evaluated at the end of each measurement batch (t_{ni}) as obtained from comparison with GPS POD products.

On the contrary, the ROD sessions on April 26, 2012 (i.e., runs 7 and 8 in Fig. 7) are affected by 2-3 times larger errors as compared to the other runs. During this phase, Mango was at separations below 10 km from the client spacecraft. Due to the predefined shutter control settings which regulate the VBS FAR image integration time, the stars were badly underexposed in the images which therefore contained only an overexposed cluster associated to Tango. Examples of these images are superimposed in Fig. 8 (right) during one of the last orbits of the ARGON experiment. It took two consecutive planning sessions (nearly one day) for the experimenter team to realize that the image processing software was not able to detect enough stars in the field of view for inertial attitude estimation (see Sect. III.B). The unavailability of this information caused a drastic reduction of angle measurements processed by ROD. After that point, the mode of operations of the software was changed to use the inertial spacecraft attitude delivered by the standard star trackers in combination with the a-priori orientation of the VBS FAR camera in the body frame [as from Eq. (8)] rather than the inertial camera attitude estimated from the VBS FAR images themselves [as from Eq. (11)]. Despite the larger bias and noise of the angle measurement residuals (see next sections), the resulting relative navigation accuracy in this so-called local mode was shown to be comparable with the previous runs of ROD in astrometry mode (see ROD runs 9 and 10 in Fig. 7).

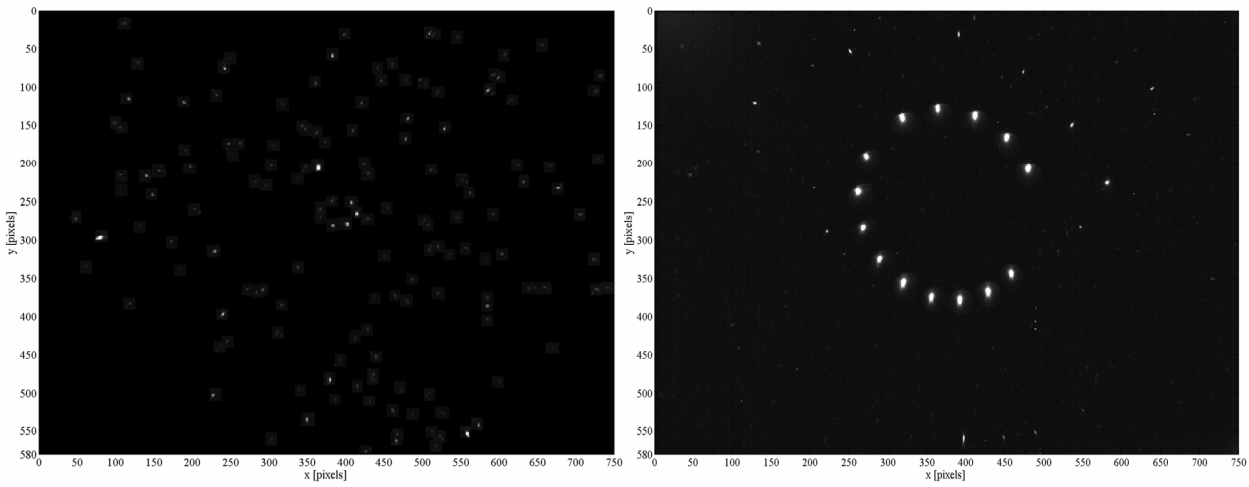

Figure 8. Superposition of ROIs taken on April 23, 15:14-16:29 (UTC) at a separation of ~30km (left) and on April 27, 18:31-19:58 (UTC) at a separation of ~3km (right).

The achieved navigation accuracy allowed a smooth rendezvous from 30 km to the final hold point at 3 km mean separation selected before the start of the experiment. Figure 9 illustrates the resulting relative motion of the servicer with respect to the client as estimated by the GPS POD after the execution of ARGON. More details on the actual behaviour and performance of IMP, ROD, and MAP during ARGON are addressed in the next dedicated sections.

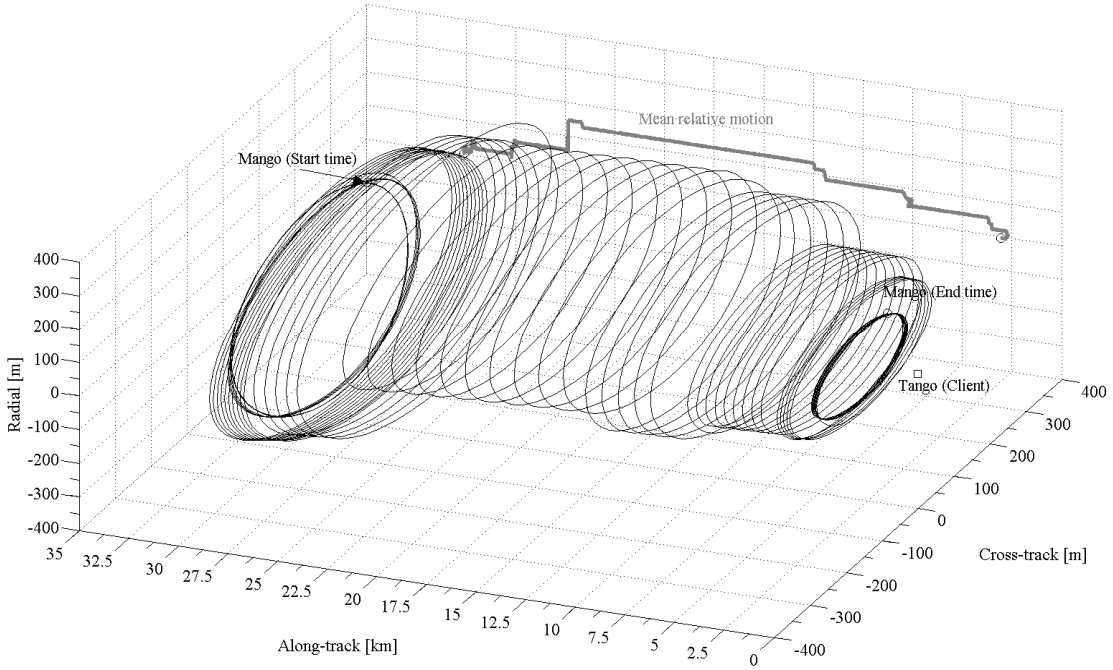

Figure 9. Actual relative position of Mango mapped in the orbital frame centered on Tango (origin) during ARGON. The true motion is provided by the GPS POD. The gray thick line represents the relative semi-major axis as a function of the mean along-track separation during the rendezvous.

B. Image Processing

The main output of the image processing software is the position of the detected client spacecraft expressed in the camera frame [i.e., $\boldsymbol{u}^c$, Eq. (10)]. Upon availability of more than 3 stars in the same image, provided that the client has been detected, IMP provides also an attitude estimate of the VBS FAR camera in the inertial frame [$\boldsymbol{R}$, Eq. (11)]. Statistics of the IMP success or hit rates during ARGON are listed in Table 5. The hit rate given in the first row is defined as the percentage of images where the target has been detected and where its measurements are flagged as continuous throughout the processed batch of images. Since IMP is normally executed after each manned

ground-contact, the single batches correspond to nearly one orbit of data sampled about every 30 s. The second row of Table 5 gives the above defined hit rate combined with the percentage of successful attitude estimates. The statistics are provided in terms of minimum and maximum hit rates encountered among all IMP runs of one day. Overall these results show how IMP is nearly always capable of detecting Tango in the images, irrespective of the image quality or VBS FAR exposure settings. On the other hand, the successful estimates of the far range camera attitude decrease substantially on April 26-27, 2012. This is due to the gradual reduction of detected stars as the servicer approaches the client spacecraft. For completeness, the average number of available stars is given by the third row of Table 5 for each day of experiment operations.

Table 5. Hit rates of image processing software during ARGON.

Item	Unit	Day				
		April-23	April-24	April-25	April-26	April-27
Client position in camera frame [$\boldsymbol{u}^c$, Eq. (10)]	[min-max %]	94.5-96.0	96.4-99.0	93.9-99.6	89.5-98.8	83.4-95.2
Combined with camera attitude [$\boldsymbol{R}$, Eq. (19)]	[min-max %]	83.9-85.0	83.9-90.2	64.8-80.8	6.9-52.0	4.5-8.7
Average number of visible stars per image [j^*, Eq. (11)]	[Nr.]	17	17	12	5	3

A fundamental functionality of the IMP module is the client centroiding algorithm described by Eq. (6). The centroiding performance has been assessed by comparing the measured client 2D position coordinates in the CCD frame (i.e., $\boldsymbol{c}^c$) with the true value derived by GPS POD. The reference relative position of Mango w.r.t. Tango is converted from the inertial frame to the camera frame through the usage of the DTU camera model (see Table 1) [29]. The computed errors and their statistics are illustrated in Fig. 10 and cover the complete ARGON experiment duration. The best centroiding performance has been achieved at the beginning of the experiment with large inter-spacecraft separations. Here the systematic errors are shown to be about 20% of the pixel size (i.e., ~16 arcsecs), whereas the standard deviation of the noise error is about 50% of the pixel size (i.e., ~40 arcsecs). Two further considerations can be made from Fig. 10.

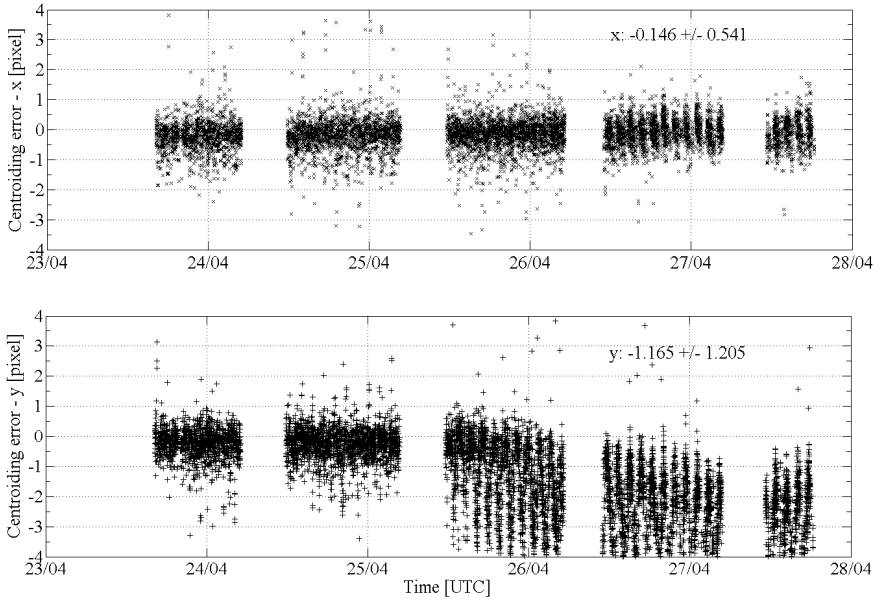

Figure 10. Client centroiding errors in x (top) and y (bottom) camera axes during ARGON experiment.

First of all, the centroiding noise is not uniformly distributed but rather exhibits a one-per-revolution error pattern. Most probably this is due to the fact that the light reflected by the imaged target depends on the illumination conditions in combination with its rotating attitude. This phenomenon is visible in Fig. 8 (left) where Tango is at about 30 km separation. Secondly, a dramatic degradation of performance is observed in the y camera axis during

the last days of the experiment (see Fig. 10 - bottom). This is due to the decreasing separation which induces an enlargement of the object size as pictured in the camera images.

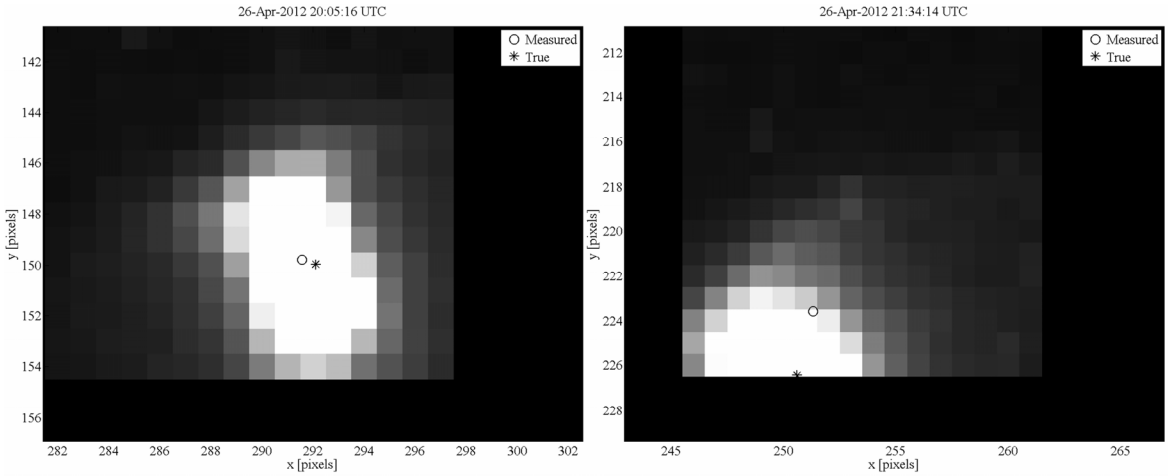

Figure 11. Examples of client centroiding errors due to small (left) and large (right) truncations of the region of interest.

This latter problem can be better understood when looking directly at ROIs provided by the camera. Figure 11 shows two examples from April 26, 2012. Here a truncation of the cluster associated to the client object is clearly visible, which in turn results in centroiding errors up to several pixels. The measured pixel coordinates are represented by a circle, whereas the object center retrieved via GPS POD is represented by a star in Fig. 11. This error seems to be dependent on the client attitude, but also on the ability of the camera to center properly the region of interest. The provided samples demonstrate that, within a limited time period (here nearly one orbit), the centroiding performance can change from a nominal (see Fig. 11 - left) to a degraded (see Fig. 11 - right) status because of truncation effects.

The image processing software has also been used to characterize the size of the cluster associated to the client object throughout the ARGON experiment. Due to the camera shutter control settings and the automatic adjustment of the image integration time, the target size is larger than the theoretical size by a factor of about 100 to 10 from 30 km to 3 km separation respectively. This result is obtained by using the DTU camera model and assuming a target spacecraft of 1m x 1m size. The theoretical size would be approximately 0.08x0.08 pixels and 0.82x0.85 pixels at 30 km and 3 km separation respectively. Although this phenomenon does not allow the estimation of the distance to the target spacecraft based on camera images only, the instrument exposure control enables angles-only navigation to the passive spacecraft over a broad dynamic range.

C. Relative Orbit Determination

Table 6 lists the main characteristics and measurement residuals statistics of each ROD session performed during ARGON. For each ROD run (labeled with tags from R1 to R10), the batch start and end time (t_{ni}) are provided, as well as the total number of valid measurements processed by ROD (i.e., 2n). In particular the runs R1-4 make use of all available measurements from experiment start until the estimation time (t_n), whereas R5-6 exploit only measurements starting from the second day of operations. Due to the phenomenon described in the previous section, the number of new valid angle observations dropped substantially from April-26, 2012. This forced the usage of all the measurements available from the beginning of the experiment during ROD runs R7-8 to avoid divergence effects. The later switch of ROD from astrometry to local mode allowed the processing of enough data to make use of only the latest available measurements during runs R9-10. The adopted thresholds for data editing and the applied a-priori standard deviation of the relative orbital elements are listed in Table 7. The magnitude of the data editing thresholds was adjusted manually at each ROD run based on the quality of the processed measurements [i.e., the rms of the measurement residuals ρ, see Eq. (23)].

The difficulty to trust the modeled observations based on the estimated state at the beginning of the experiment prevented the setting of reasonable data editing thresholds during the R1 iterations. In fact no maneuvers took place

during the involved data arc and a coarse a-priori state was derived from TLE navigation. Tight data editing thresholds down to 80 arcsecs (i.e., ~1 pixel) were successfully applied during runs R2-6. On the contrary, these limits had to be enlarged during runs R7-8 due the lack of new valid measurements. Typical maximum acceptable magnitudes of the residuals of 400 arcsecs were reestablished within runs R9-10 until the end of the experiment.

The a-priori standard deviation of R1 represents the typical confidence that the available initial conditions computed via TLE can guarantee (see Sect. III.E, Table 2). The a-priori standard deviation of $a\delta u$ was artificially set to a smaller value as compared to the other elements. This was motivated by the fact that no maneuvers took place during the involved data arc, thus reducing the degree of observability of the dynamic system. By constraining the mean along-track separation, the least-squares filter could only act on the remaining parameters which define the projection of the relative motion in the radial/cross-track (RN) plane. Given the Mango attitude, the VBS camera boresight direction, and the tangential separation at the beginning of the rendezvous, the RN plane almost coincides with the camera CCD plane. As a consequence, the ROD fitting was able to identify the relative orbit shape except for a scale factor related to the ambiguity in $a\delta a$ and $a\delta u$. Irrespective of this deficiency, the angles-only relative orbit determination managed to accurately adjust $a\delta \boldsymbol{e}$ and $a\delta \boldsymbol{i}$, which were originally affected by the largest error due to the TLE navigation. During R2-4, the formal a-priori standard deviation of the state solution from the previous run was applied. From R5 onwards, the a-priori standard deviation corresponds to a very poor confidence on the initial guess. The strategy was to leave enough freedom to the ROD filter in order to act on all relative orbital elements.

Table 6. Summary of ROD runs and resulting measurement residuals statistics during ARGON

ROD run	Start time [UTC]	End time [UTC]	Total nr. of measurements	Azimuth residuals mean±std [arcsecs]	Elevation residuals mean±std [arcsecs]
R1	23/04 14:31:31	23/04 15:59:20	300	0.01 ± 39.59	-10.78 ± 39.83
R2	23/04 14:31:31	23/04 19:27:43	976	-0.72 ± 21.03	7.01 ± 17.56
R3	23/04 14:31:31	24/04 13:39:17	2998	0.01 ±13.46	9.70 ± 15.73
R4	23/04 14:31:31	24/04 18:47:37	4272	0.43 ± 18.85	8.83 ± 14.82
R5	24/04 14:00:08	25/04 14:39:06	3596	-0.80 ± 17.73	3.15 ± 29.83
R6	24/04 14:00:08	25/04 21:46:22	5014	2.27 ± 21.87	3.21 ± 22.70
R7	23/04 14:31:31	26/04 13:56:36	9842	17.58 ± 79.62	-7.44 ± 51.47
R8	23/04 14:31:31	26/04 20:24:32	10202	15.61 ± 133.59	-33.88 ± 107.07
R9	25/04 14:00:25	27/04 13:19:00	12658	23.89 ± 87.38	-30.31 ± 136.39
R10	26/04 13:59:51	27/04 18:19:18	9072	2.93 ± 87.62	-82.99 ± 109.32

The statistics of the measurement residuals given in Table 6 reflects the ROD mode of operations and the overall trend described in the previous section. In particular the residual offset stays below 10 arcsecs when enough inertial attitude estimates of the VBS FAR camera are available (i.e., R1-6). As soon as the measurements are processed through inconsistent attitude information delivered by the standard star trackers, and in the presence of ROI truncation effects, the residual bias increases up to 80 arcsecs. Similarly, the noise of the measurements computed by ROD increases from 20-30 arcsecs at the beginning of ARGON to 90-100 arcsecs when the separation gets smaller than approximately 10 km. It is noted that the weight of the angle measurements in ROD has been kept constant during ARGON with a value of $\sigma_\eta = \sigma_\psi = 40$ arcsecs (i.e., ~0.5 pixel).

The most important output of ROD is the estimate of the relative orbital elements at the end time of each measurements batch (c.f., Table 6 - End time). Although the accuracy of these estimates has already been assessed through Fig. 7, interesting remarks can be made now in view of the obtained measurement residuals. An angular error of 40 arcsecs maps to relative position errors of the order of 6 m at 30 km separation. Similarly, angular errors of 120 arcsecs map to relative position errors of the order of 1.8 m at 3 km separation. This trend seems to be reflected in the observable relative orbital elements (i.e., excluding $a\delta u$). Overall, despite the degradation of the measurement quality, the relative navigation accuracy tends to improve (or remain constant) for smaller separations due to the better geometry conditions. Obviously these considerations exclude the degraded ROD runs R7-8 which were predominantly affected by the reduced number of valid measurements.

It is interesting to evaluate how well the relative orbit estimated by ROD compares to the truth during the complete measurements or orbit determination arc. The ROD output estimate is back propagated to the time of each processed measurement using the same model applied within the batch least-squares filter [see Eq. (13)]. The resulting states are subtracted from the actual relative orbital elements computed from the GPS POD products to obtain the relative orbit determination errors at the same times. This process has been repeated for each ROD session. Such an evaluation is offered by Fig. 12 (bottom) for one of the state parameters, namely the relative semi-major axis. Evidently the relative semi-major axis which best fits the available measurements in a least-squares sense is affected by an error which increases linearly with time. This phenomenon reveals a possible deficiency of the adopted linear relative orbit model which neglects differential drag effects.

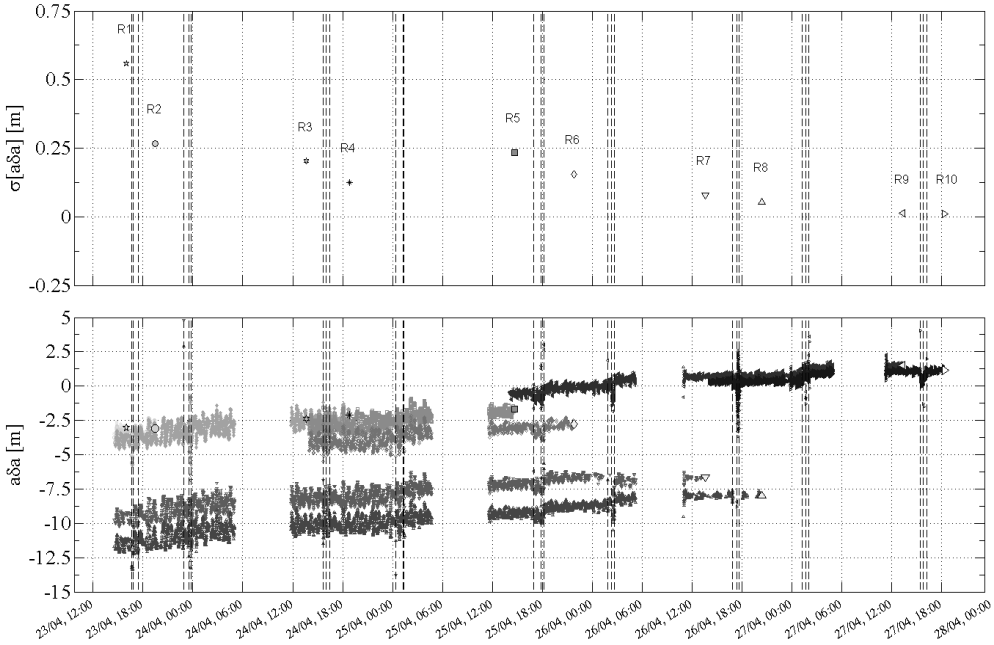

Figure 12. Relative orbit determination errors for the relative semi-major axis as obtained from comparison with GPS POD products (bottom). Formal standard deviation evaluated at estimation time, i.e., at the end of each measurement batch (top). Each ROD session is indicated by a different color and symbol. Dashed vertical lines represent orbit control maneuvers.

Fig. 12 (top) illustrates also the formal standard deviation of the estimated state, $\sigma[\boldsymbol{x}^{lsq}]$, as computed by ROD. The values are shown to be one order of magnitude smaller than the actual errors and could not be used for proper assessments of the angles-only navigation accuracy during ARGON. The standard deviation is also gradually reducing throughout the experiment due to the accumulation of an increasingly large number of measurements and due to the improved observability. Furthermore no evidence is given of the encountered anomaly on April 26, since the large majority of measurements refer to the previous days.

Table 7. Summary of ROD data editing thresholds and a-priori state standard deviation during ARGON

	Data editing [arcsecs]					A-priori state standard deviation [m]					
Iteration	1	2	3	4	5	$a^o\delta a$	$a^o\delta e_x$	$a^o\delta e_y$	$a^o\delta i_x$	$a^o\delta i_y$	$a^o\delta u$
R1	-	-	-	-	-	20.0	100.0	100.0	100.0	100.0	10.0
R2	100	100	100	100	100	0.6	0.7	0.8	0.8	0.7	10.0
R3	1000	250	70	70	70	1.3	1.9	1.9	1.9	1.9	50.0
R4	1000	250	70	70	50	0.2	0.2	0.5	0.2	0.4	43.9
R5	1000	250	150	150	150	50	100	100	100	100	1000
R6	1000	250	150	80	80	50	100	100	100	100	1000
R7	10000	3000	1000	400	200	50	100	100	100	100	1000
R8	1000	1000	1000	1000	1000	50	100	100	100	100	1000
R9	4000	4000	4000	500	400	50	100	100	100	100	1000
R10	1000	1000	1000	500	400	50	100	100	100	100	1000

D. Maneuver Planning

The MAP on-orbit results are summarized by Fig. 13 and Table 8. Figure 13 illustrates the actual relative orbital elements acquired and kept during the ARGON experiment as from the GPS POD. The ROD output state estimates used by each maneuver planning session are superimposed on the same figure. Table 8 lists the statistics of the control tracking errors which are computed as the difference between the desired formation configurations and the POD results.

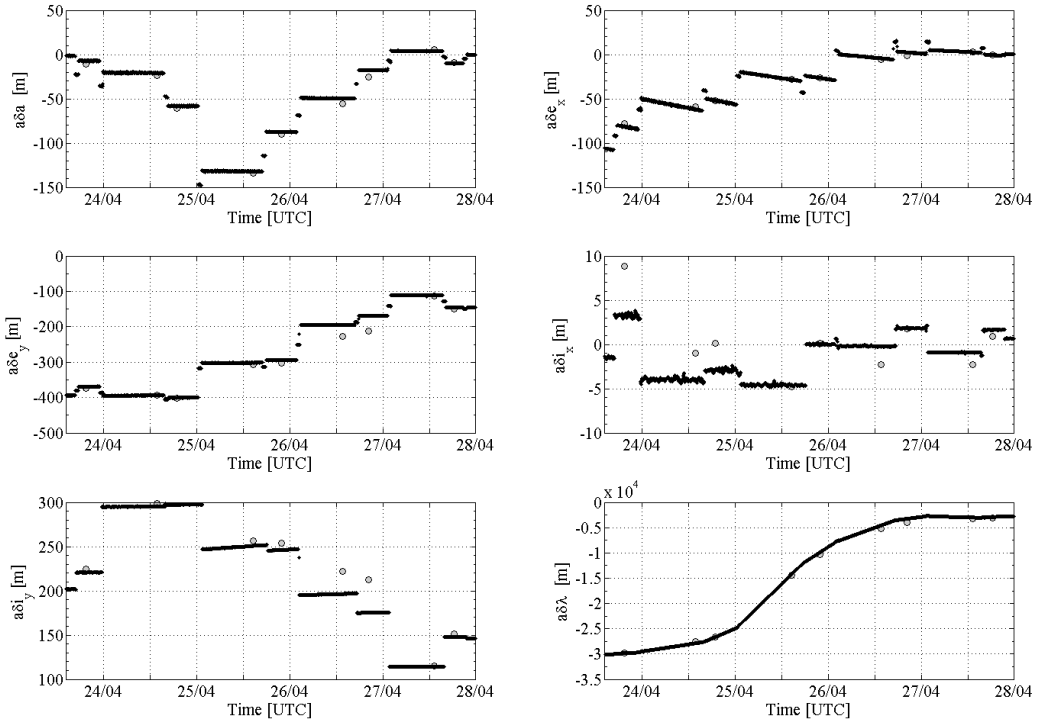

Figure 13. True relative orbit elements as obtained from GPS POD products (black line) and state estimates from relative orbit determination for maneuver planning (gray circles).

The relative eccentricity and inclination vectors have been properly aligned in a safe anti-parallel configuration in a step-wise manner throughout the experiment (see $a\delta e_x$ and $a\delta i_x$ components approaching zero in Fig. 13). The magnitude of the radial and cross-track oscillations has been decreased from ca. 300-400 m to 150 m at the end configuration to always keep Tango in the camera field of view and, at the same time, guarantee a minimum separation perpendicular to the flight direction at all times. A large increment of $a\delta i_y$ from 220 m to 300 m is visible on April 24. This was intended to recover errors of the initial formation configuration (due to TLE-navigation) which was characterized by an amplitude of the relative inclination vector considered too small as compared with the guidance profile. The relative semi-major axis has been gradually decreased to ca. -140 m (see Fig. 13 – top/left) to establish the maximum drift (ca. -1.5 km/orbit) on April 25, 2012 (see Fig. 13 – bottom/right), and progressively increased to its final value around -0.4 m at the end of ARGON on April-27, 2012 - 21:40 UTC. The mean along-track separation was affected by a control error of about 300 m throughout the rendezvous, i.e. 1% of the initial separation. The amplitude of the relative eccentricity and inclination vectors deviated by less than 20 m (rms) from the desired values. It is noted that the rendezvous performance has been slightly degraded by the decrease of navigation accuracy on April 26 as explained in the previous section (see Fig. 10, bottom). The overestimation of the relative semi-major axis induced a temporary drift of Mango w.r.t. Tango in along-track direction (i.e., opposite to nominal) and small undesired changes of the relative eccentricity and inclination vectors. These latter are visible in Fig. 13 where $a\delta e_y$ and $a\delta i_y$ approach absolute values of 110 m on the morning of April 27. The control accuracy got back to normal values in the afternoon, after the first maneuver planning session of the day. This allowed the acquisition of the aimed final formation geometry within the expected error margins at the end of the experiment. The total delta-v consumed during ARGON has been approximately 1 m/s, i.e., half of the originally allocated budget.

Table 8. Control errors computed as difference between desired and true relative orbital elements.

Parameter	Control errors during ARGON		
	Mean [m]	Standard deviation [m]	Root-Mean-Square [m]
$a^o\delta a$	-3.1	4.3	5.3
$a^o\delta e_x$	-0.4	4.1	4.1
$a^o\delta e_y$	-11.2	15.2	18.9
$a^o\delta i_x$	1.6	2.3	2.8
$a^o\delta i_y$	10.6	12.7	16.5
$a^o\delta\lambda$	-61.9	312.9	319.0

VI. CONCLUSIONS

This paper has presented system design and flight results from ARGON, one of the first demonstrations documented in the published literature of non-cooperative far-range rendezvous in low Earth orbit based on angles-only measurements. For the first time, specifically developed techniques and software modules have been exercised during actual mission operations in a ground-in-the-loop fashion. These include routine image processing, angles-only relative orbit determination, guidance and maneuver planning, among others. In contrast to previous flight demonstrations, ARGON is a fully non-cooperative experiment where neither knowledge nor control of the client vehicle is available during execution. The technology presented in this paper could demonstrate a reliable, safe and accurate far-range approach to a passively rotating vehicle using angles-only measurements for navigation and relative eccentricity/inclination vectors for guidance and control. In addition, the post-facto availability of independent and accurate navigation information coming from relative GPS gave the possibility to properly evaluate the achieved navigation and control accuracies.

Although a big effort has been put into the generalization of the ARGON scenario for its future applicability to other missions, four relevant items need to be mentioned here for future assessment. First of all the accuracy of the angles-only relative navigation is strictly dependent on the adopted camera hardware, its resolution, and an appropriate bias calibration. In the PRISMA case, the Vision-Based Sensor (VBS) far-range camera has a resolution of 752x580 pixels and half field of view of 9.15x6.85 deg, which provide a pixel size of ca. 80 arcsecs. This drives the noise of the line-of-sight measurements which has been found to be 20% of the pixel size (~16 arcsecs) at its best. A simple star tracker camera calibration model has been adopted to take into account effects such as lens distortion, non-quadratism and offsets between optical and geometric axes which accounts for measurement biases up to 1-2 pixels. As a result, residual systematic offsets of the order of 40 arcsecs (~50% of pixel size) have been achieved at large separations (> 10 km). In order to further improve the quality of the measurements, an effort should be put into the improvement of the centroiding function and its integration within an on-line calibration process. Residual distortion effects could be mitigated through a refinement of the camera model itself, e.g. taking into account higher order, or temperature dependent terms, among others. It is believed that such improvements could reduce the client centroiding rms errors to better than 0.2 pixel.

Second, due to the limitations encountered with the servicer telemetry data-rate budget, only so-called regions of interest (ROIs) extracted from raw camera images could be downloaded and used for navigation during ARGON. The ROIs result from a basic image processing performed by the on-board system which is out of user control. On one hand, this simplifies the image processing performed on ground which is asked to process only 10-15 ROIs per image. On the other hand, the generated ROIs have a limited size and are often subject to overflow effects where a substantial area of the light cluster associated to the client is cut off. This phenomenon causes undesirable biases in the extracted measurements, especially at close separations, which are difficult if not impossible to estimate. More investigations should focus on the analysis of complete images collected during ARGON and on the assessment of the measurement quality as compared to the ROIs.

Third, the illumination conditions of the ARGON experiment have to be considered. The observed once-per-revolution pattern of the angle measurement residuals suggests that the attitude motion of the client affects significantly the shape of the light cluster as pictured by the camera. This may contribute to the illumination of camera pixels in the neighborhood of the target whose shape appears about 10 to 100 times bigger than theoretically expected due the camera defocusing. This makes the estimation of the range to target based on apparent diameter measurements, as suggested by various authors, totally unreliable. Because of the specific PRISMA orbit, the Sun is nearly perpendicular to the orbital plane and neither eclipses nor intrusions of the Moon in the field of view were

experienced during ARGON. On the other hand, data gaps of at least 7 hours per day were induced by the specific telemetry configuration. These did not affect the navigation and control performance during the rendezvous and suggest that eventual illumination constraints can be handled in a similar manner.

Last but not least, the achievable relative navigation accuracy is affected by the adopted processing scheme and by issues of observability. Given the aforementioned camera measurements, relative navigation errors below 3-10 m could be demonstrated throughout the complete rendezvous (i.e., from 30 km down to 3 km separation) on all relative orbital elements, excluded the relative mean argument of latitude. Despite the execution of regular and diverse orbit control maneuvers to obtain an unambiguous set of measurements, the mean along-track separation remained affected by errors substantially larger than what is feasible through radar or lidar tracking. This intrinsic limitation of angles-only relative navigation calls for a deeper analysis of the guidance profile which should be specifically optimized for navigation accuracy. Furthermore alternative filtering schemes could be investigated such as consider covariance techniques which are able to select optimum sets of observations for best observability. These approaches may also be able to improve the estimation of the formal covariance which has shown not to be representative of the actual state errors.

Despite the aforementioned limitations, this work has not only shown the viability of angles-only navigation for long-term rendezvous operations, but also its high technology readiness level through its simplicity and robustness. The technology developed and demonstrated during ARGON will find relevant applications in present and future missions which foresee DLR/GSOC involvement. Key examples are on-orbit servicing satellites such as DEOS, technology demonstrators such as BIROS, and active debris removers which are being studied by ESA and DLR to reentry satellites in sun-synchronous orbits. Ultimately the intention is to transfer the ARGON technology to a servicer spacecraft in order to perform fully autonomous vision-based rendezvous to a non-cooperative target.

Acknowledgments

The authors would like to thank Thomas Karlsson, Robin Larsson, and Eric Clacey of OHB-SE for the support and conduction of the ARGON experiment on the PRISMA mission.

References

[1]Weismuller, T., and Leinz, M., "GN&C Technology Demonstrated by the Orbital Express Autonomous Rendezvous and Capture Sensor System," AAS Paper 06-016, 2006.

[2]Rupp, T., Boge, T., Kiehling, R., Sellmaier, F., "Flight Dynamics Challenges of the German On-Orbit Servicing Mission DEOS," 21st International Symposium on Space Flight Dynamics (ISSFD), 28 Sep. - 2 Oct. 2009, Toulouse, France, 2009.

[3]Ardaens, J.-S., D'Amico, S., Fischer, D., "Early Flight Results from the TanDEM-X Autonomous Formation Flying System," 4th International Conference on Spacecraft Formation Flying Missions & Technologies (SFFMT), 18-20 May 2011, St-Hubert, Quebec, 2011.

[4]D'Amico, S., Ardaens, J.-S., Larsson, R., "Spaceborne Autonomous Formation-Flying Experiment on the PRISMA Mission," *Journal of Guidance, Control, and Dynamics* 2012, 0731-5090, vol.35 no. 3 (834-850), May-June 2012, doi: 10.2514/1.55638.

[5]Woffinden, D.C., and Geller, D.K., "Navigating the Road to Autonomous Orbital Rendezvous," *Journal of Spacecraft and Rockets* 2007, vol. 44, no. 4 (898-909), July–August 2007, doi: 10.2514/1.30734.

[6]Chari, R. J. V., "Autonomous Orbital Rendezvous Using Angles-Only Navigation," Master's thesis, Massachusetts Institute of Technology, June 2001.

[7]Jørgensen, J.L., Denver, T., Jørgensen, P.S., "Using an Autonomous Star Tracker as Formation Flying Sensor", 4th Symposium on Small Satellites Systems and Services, Sept. 20-24, La Rochelle, France, 2004.

[8]Woffinden, D.C., "On Orbit Satellite Inspection," Master's thesis, Massachusetts Institute of Technology, Cambridge, MA, 2004.

[9]Schmidt, J., Geller, D.K., Chavez, F., "Viability of Angles-only Navigation for Orbital Rendezvous Operation," AIAA 2010-7755, AIAA Guidance, Navigation, and Control Conference, 2-5 August 2010, Toronto, Ontario Canada, 2010.

[10]Patel, H., Lovell, T.A., Allgeier, S., Russel, R, Sinclair, A., "Relative Navigation for Satellites In Close Proximity using Angles-only Observations," AAS 12-202, AAS/AIAA Space Flight Mechanics Meeting, Charleston, SC, Jan 2012.

[11]Noteborn, R., Bodin, P., Larsson, R., Chasset, C., "Flight Results from the PRISMA Optical Line of Sight Based Autonomous Rendezvous Experiment," 4th International Conference on Spacecraft Formation Flying Missions & Technologies (SFFMT), 18-20 May 2011, St-Hubert, Quebec, 2011.

[12]Delpech, M, Berges, J.C., Djalal, S., Guidotti, P.Y., and Christy, J., "Preliminary Results of the Vision Based Rendezvous and Formation Flying Experiments Performed During the Prisma Extended Mission," IAA-AAS-DyCoSS1-12-07, 1st IAA Conference on Dynamics and Control of Space Systems, DyCoSS' 2012, Porto, Portugal, March 2012.

[13]Bodin, P., Noteborn, R., Larsson, R., Karlsson, T., D'Amico, S., Ardaens, J.-S., Delpech, M., Berges, J.-C., "Prisma Formation Flying Demonstrator: Overview and Conclusions from the Nominal Mission," AAS 12-072; 35th Annual AAS Guidance and Control Conference, 3-8 Feb. 2012, Breckenridge, Colorado (2012).

[14]Kelso, T.S., "Validation of SGP4 and IS-GPS-200D Against GPS Precision Ephemerides," AAS paper 07-127, 17th AAS/AIAA Space Flight Mechanics Conference, Sedona, AZ, January 29, 2007.

[15]Ardaens, J.-S., D'Amico, S., Montenbruck, O., "Final Commissioning of the PRISMA GPS Navigation System," 22nd International Symposium on Spaceflight Dynamics (ISSFD), 28 Feb. - 4 March 2011, Sao Jose dos Campos, Brazil (2011).

[16]D'Amico, S., Montenbruck, O., "Proximity Operations of Formation Flying Spacecraft using an Eccentricity/Inclination Vector Separation," AIAA Journal of Guidance, Control and Dynamics, 29/3 554-563 (2006).
[17]Gaias, G., D'Amico, S., Ardaens, J.-S., "Angles-only Navigation to a Non-Cooperative Satellite using Relative Orbital Elements," AIAA/AAS Astrodynamics Specialists Conference, Minneapolis, MN, 13-16 August 2012.
[18]D'Amico, S., "Autonomous Formation Flying in Low Earth Orbit," PhD thesis, Technical University of Delft, March 2010.
[19]Micheau, P., "Spaceflight Dynamics – Orbit Control Techniques for Low Earth Orbiting (LEO) Satellites," Chapter 13. Cepadues-Editions, edited by J.P. Carrou, 1995.
[20]Hill, G.W., "Researches in the Lunar Theory," American Journal of Mathematics, 1:5-26, 1878.
[21]Montenbruck, O., and Gill, E., "Satellites Orbits – Models, Methods, and Applications," Springer Verlag, Heidelberg, Germany, 2001a.
[22]Woffinden, D.C., Geller, D.K., "Observability Criteria for Angles-Only Navigation," IEEE Transactions on Aerospace and Electronic Systems, 45/3 1194-1208, July 2009.
[23]Persson, S., Veldman, S., and Bodin, P., "PRISMA—A Formation Flying Project in Implementation Phase," Acta Astronautica, Vol. 65, Nos. 9–10, 2009, pp. 1360–1374. doi:10.1016/j.actaastro.2009.03.067.
[24]Bodin, P., Larsson, R., Nilsson, F., Chasset, C., Noteborn, R., and Nylund, M., "PRISMA: An In-Orbit Test Bed for Guidance, Navigation, and Control Experiments," Journal of Spacecraft and Rockets, Vol. 46, No. 3, 2009, pp. 615–623. doi:10.2514/1.40161.
[25]Carlsson, A., "A General Control System for Both Sounding Rockets and Satellites," 18th ESA symposium on European Rockets an Balloon Programmes and Related Research, Visby, June 3-7, 2007.
[26]Karlsson, T., Ahlgren, N., Faller, R., and Schlepp, B., "PRISMA Mission Control: Transferring Satellite Control between Organisations", Submitted to SpaceOps 2012, 11-15 June, Stockholm, Sweden, 2012.
[27]Jørgensen, J. L., Benn, M., "VBS - The Optical Rendezvous and Docking Sensor for PRISMA," In: NordicSpace, 2010, p. 16-19.
[28]Wertz, J.R., "Spacecraft Attitude Determination and Control," p.414, Kluwer Academic Publisher, 1997.
[29]Benn, M., Denver, T.," Advanced Stellar Compass - Lens Distortion Correction Method for the μASC," ASC-DTU-MA-3013, Issue 1.0, March 19, 2012.
[30]Clohessy, W. H., and Wiltshire, R. S., "Terminal Guidance System for Satellite Rendezvous," Journal of the Aerospace Sciences, Vol. 27, 1960, pp. 653–658.
[31]ESA, Hipparcos Space Astrometry Mission, http://www.rssd.esa.int/index.php?project=HIPPARCOS.
[32]Wermuth, M., Montenbruck, O., van Hellepute, T., "GPS High Precision Orbit Determination Software Tools (GHOST)," 4th International Conference on Astrodynamics Tools and Techniques, 3-6 May 2010, Madrid (2010).
[33]Brower, D., "Solution of the problem of artificial satellite theory without drag," Astronomical Journal, 64(1274): 378-397 (1959).
[34]Woffinden, D.C., Geller, D.K., "Optimal Orbital Rendezvous Maneuvering for Angles-Only Navigation," Journal of Guidance, Control, and Dynamics, Vol. 32, No. 4, pp. 1382-1387, July–August 2009.
[35]Demeuse, B., Valera, S., "PLUTO, a Procedure Language for Users in Test and Operations," DASIA 98 - Data Systems in Aerospace, Proceedings of the conference held 25-28 May, 1998 in Athens, Greece. Edited by B. Kaldeich-Schü.rmann. ESA SP-422. Paris: European Space Agency, 1998., p.307, 07/1998.
[36]Yunck, T.P., "Coping with the Atmosphere and Ionosphere in Precise Satellite and Ground Positioning," in Environmental Effects on Spacecraft Positioning and Trajectories, Geophys. Monograph 73, IUGG v. 13, 1993
[37]Montenbruck, O., Issler, J.-L., Markgraf, M., Mercier, F., Santandrea, S., Garcia, A., Naudet, J., Serre, S., "GPS Based Precise Orbit Determination and Real-Time Navigation of the PROBA-2 Spacecraft," 5th ESA Workshop on Satellite Navigation Technologies, NAVITEC'2010, 8-10 Dec. 2010, Noordwijk, Netherlands (2010).
[38]Hoots, F. R., and Roehrich, R. L., "Spacetrack Report No. 3: Models for Propagation of the NORAD Element Sets," U.S. Air Force Aerospace Defense Command, Colorado Springs, CO, 1980.
[39]Spurmann, J., D'Amico, S., "Proximity Operations of On-Orbit Servicing Spacecraft using an Eccentricity/Inclination Vector Separation," 22nd International Symposium on Spaceflight Dynamics, 28 Feb. - 4 Mar. 2011, Sao Jose dos Campos, Brazil (2011).